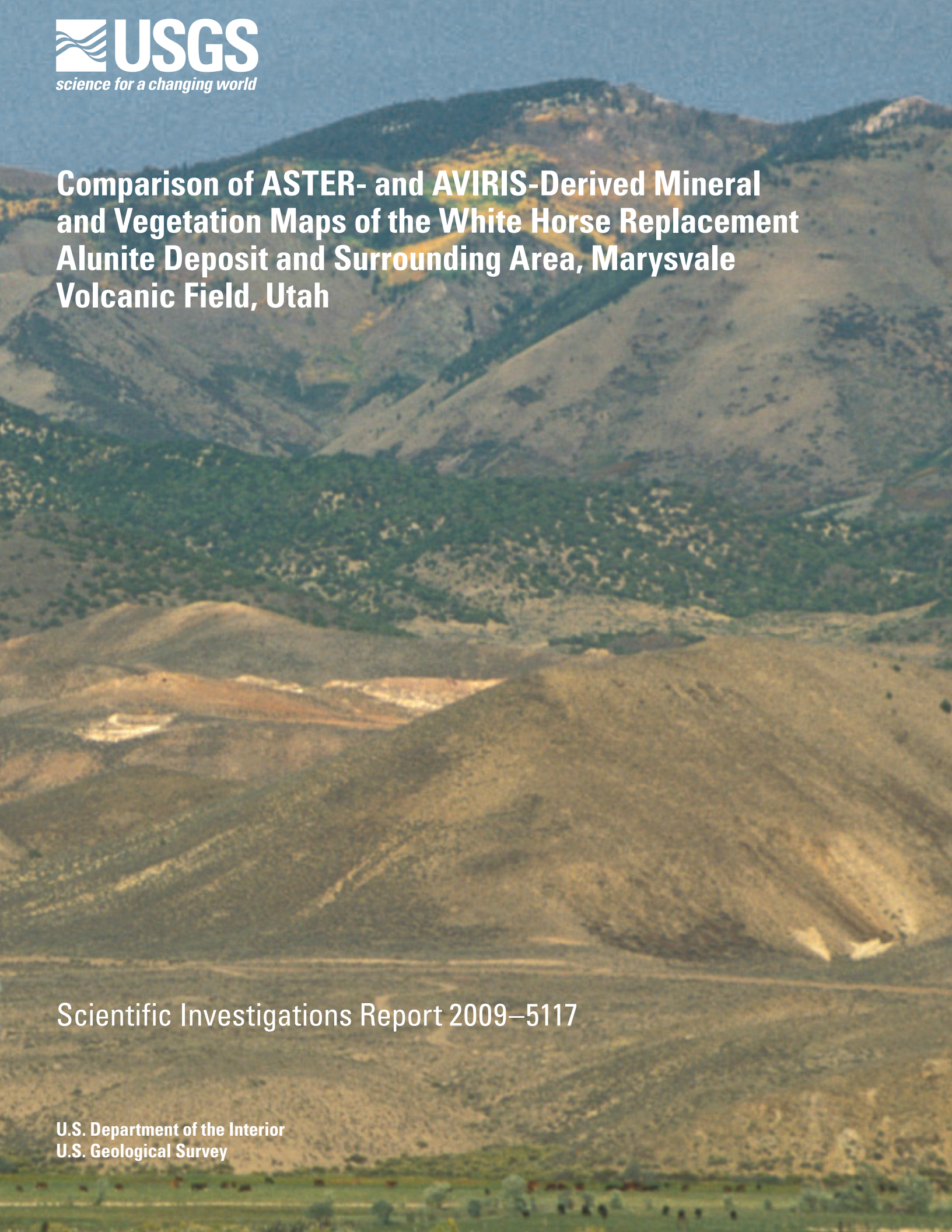


USGS
science for a changing world

Comparison of ASTER- and AVIRIS-Derived Mineral and Vegetation Maps of the White Horse Replacement Alunite Deposit and Surrounding Area, Marysvale Volcanic Field, Utah

Scientific Investigations Report 2009–5117

U.S. Department of the Interior
U.S. Geological Survey



FRONT COVER: View of the White Horse mine (bright rocks at center) from the Sevier River flood plain with Marysvale Peak on the skyline, looking toward the east. The subhorizontal bulldozer cuts above and behind the mine mark the White Hills alunite deposit. The summit of Marysvale Peak is underlain by another alunite deposit. The bright, buff-colored cliffs at left center are an exposure of hydrothermally altered volcaniclastic sedimentary rocks and related flows (unit Tmps) that are discussed in the text. Argillically altered rocks of the Saturday uranium prospect are visible at extreme right center within the northern Bullion Hills. The entire area visible in the photograph lies within the inferred boundary of the Monroe Peak caldera.

Comparison of ASTER- and AVIRIS-Derived Mineral and Vegetation Maps of the White Horse Replacement Alunite Deposit and Surrounding Area, Marysvale Volcanic Field, Utah

By Barnaby W. Rockwell

Scientific Investigations Report 2009–5117

U.S. Department of the Interior
U.S. Geological Survey

U.S. Department of the Interior
KEN SALAZAR, Secretary

U.S. Geological Survey
Suzette M. Kimball, Acting Director

U.S. Geological Survey, Reston, Virginia: 2009

For product and ordering information:
World Wide Web: http://www.usgs.gov/pubprod
Telephone: 1-888-ASK-USGS

For more information on the USGS--the Federal source for science about the Earth, its natural and living resources, natural hazards, and the environment:
World Wide Web: http://www.usgs.gov
Telephone: 1-888-ASK-USGS

Any use of trade, product, or firm names is for descriptive purposes only and does not imply endorsement by the U.S. Government.

Although this report is in the public domain, permission must be secured from the individual copyright owners to reproduce any copyrighted materials contained within this report.

Suggested citation:
Rockwell, B.W., 2009, Comparison of ASTER- and AVIRIS-derived mineral and vegetation maps of the White Horse replacement alunite deposit and surrounding area, Marysvale volcanic field, Utah: U.S. Geological Survey Scientific Investigations Report 2009–5117, 31 p.

Contents

Abstract....1
Introduction....2
Geographic and Geologic Setting of the White Horse Mine and Surrounding Area....2
Mineral and Vegetation Maps Derived from AVIRIS data....6
Processing and Analysis of ASTER Data....10
Mineral and Vegetation Maps Derived from ASTER Data....12
False-Color Composite Image—Vegetation, Snow, and Surface Albedo....12
Visible and Near-Infrared Mapping—Iron Minerals....12
Vegetation....16
Shortwave-Infrared Mapping and Detector "Scratch"....16
Advanced Argillic Alteration and Areal Mixing....19
Phyllic Alteration and Pyrophyllite....19
Carbonate....20
Epidote....20
Sericites....21
Argillic Alteration in Quartz Arenites....21
Kandite Clay Differentiation....22
Comparison of AVIRIS- and ASTER-Derived Mineral Maps....25
Conclusions....29
Acknowledgments....29
References....29

Figures

1. Index map of study area showing footprints of ASTER data, high-altitude AVIRIS data, low-altitude AVIRIS data, and geologic map shown in figure 3....3
2. Perspective view of the Antelope Range area looking toward the northeast....4
3. Geologic map of southern Antelope Range and surrounding area....5
4. True-color composite of AVIRIS flightline over White Horse deposit....7
5. Map of iron-bearing minerals and water generated from AVIRIS data in the 0.35–1.35-micrometer region....8
6. Map of clay, sulfate, mica, carbonate, and Mg-OH minerals generated from AVIRIS data in the 1.45–2.50-micrometer region....9
7. Averaged AVIRIS spectra of vegetation classes....10
8. Map of vegetation vigor and dryness generated from AVIRIS data....11
9. Map showing ASTER 431/RGB false-color composite image of the Marysvale region....13
10. Plot of selected convolved laboratory spectra of iron-bearing minerals, vegetation, and water (on left) used as references for analysis of ASTER data....14
11. Map of iron-bearing minerals, vegetation, and water derived from spectral analysis of ASTER data....15

12. Plot of selected convolved laboratory spectra of clay, sulfate, mica, carbonate, and sorosilicate (epidote) minerals and mineral mixtures having diagnostic SWIR absorption features used as references for analysis of ASTER data....17
13. Map of clay, sulfate, mica, hydrous quartz, carbonate, and Mg-OH minerals derived from spectral analysis of ASTER shortwave infrared (SWIR) data 18
14. Shortwave infrared spectral plots of dickite and well-crystallized kaolinite from Clark and others (2003b) convolved to ASTER spectral resolution....22
15. Map of clay, sulfate, mica, hydrous quartz, carbonate, and Mg-OH minerals derived from spectral analysis of ASTER shortwave infrared (SWIR) data with dickite added as a reference spectrum....23
16. Results of ASTER band depth analysis of mineral identification results shown in figure 13 over the Yellow Jacket and Al Kee Mee replacement alunite deposits in the Antelope Range....24
17. Map of alunites and kandite clay minerals derived from spectral analysis of ASTER shortwave infrared (SWIR) data....26
18. Mineral map from figure 13 merged with results of kandite clay differentiation based on band-depth analysis....27
19. Comparison of shortwave infrared (SWIR) mineral maps derived from AVIRIS and ASTER data....28

Table

1. Measured spectral performance of ASTER VIS, NIR, and SWIR bands.....12

Comparison of ASTER- and AVIRIS-Derived Mineral and Vegetation Maps of the White Horse Replacement Alunite Deposit and Surrounding Area, Marysvale Volcanic Field, Utah

Barnaby W. Rockwell

Abstract

This report presents and compares mineral and vegetation maps of parts of the Marysvale volcanic field in west-central Utah that were published in a recent paper describing the White Horse replacement alunite deposit. Detailed, field-verified maps of the deposit were produced from Airborne Visible/Infrared Imaging Spectrometer (AVIRIS) data acquired from a low-altitude Twin Otter turboprop airborne platform. Reconnaissance-level maps of surrounding areas including the central and northern Tushar Mountains, Pahvant Range, and portions of the Sevier Plateau to the east were produced from visible, near-infrared, and shortwave-infrared data acquired by the Advanced Spaceborne Thermal Emission and Reflection Radiometer (ASTER) sensor carried aboard the Terra satellite platform. These maps are also compared to a previously published mineral map of the same area generated from AVIRIS data acquired from the high-altitude NASA ER–2 jet platform. All of the maps were generated by similar analysis methods, enabling the direct comparison of the spatial scale and mineral composition of surface geologic features that can be identified using the three types of remote sensing data.

The high spatial (2–17 meters) and spectral (224 bands) resolution AVIRIS data can be used to generate detailed mineral and vegetation maps suitable for geologic and geoenvironmental studies of individual deposits, mines, and smelters. The lower spatial (15–30 meters) and spectral (9 bands) resolution ASTER data are better suited to less detailed mineralogical studies of lithology and alteration across entire hydrothermal systems and mining districts, including regional mineral resource and geoenvironmental assessments. The results presented here demonstrate that minerals and mineral mixtures can be directly identified using AVIRIS and ASTER data to elucidate spatial patterns of mineralogic zonation; AVIRIS data can enable the generation of maps with significantly greater detail and accuracy. The vegetation mapping results suggest that ASTER data may provide an efficient alternative to spectroscopic data for studies of burn severity after wildland fires.

The AVIRIS-derived maps were produced through the quantitative comparison of continuum-removed image spectra and laboratory reference spectra by using previously described least-squares curve-fitting techniques. The ASTER-derived maps presented here were produced by a similar methodology adapted for analysis of ASTER multispectral data. This semi-automated methodology is currently being applied to ASTER data coverage of large areas for regional assessments of mineral-resource potential and mineral-environmental effects. While legacy multispectral data such as those acquired by the spaceborne Landsat Thematic Mapper sensor can detect large hydrothermally altered areas, ASTER data can further characterize the alteration in those areas by discriminating specific minerals such as sericite, kaolinite, smectite, alunite, gypsum, calcite, dolomite, epidote, hydrous quartz (opal or chalcedony), ferrous iron minerals, ferric iron minerals including spectrally pure jarosite and copiapite, and certain mixtures of these minerals. Compared to spectroscopic remote sensing data, however, the large pixels and multispectral nature of ASTER data necessarily increase the effects of areal mixing of materials within a pixel and reduce the uniqueness of image spectra when materials with overlapping absorption features coexist within a pixel. Both of these effects result in a lower confidence level for spectral identifications derived from ASTER data.

In the replacement alunite deposits, the AVIRIS data were used to identify halos of argillically altered rocks containing quartz + dickite ± kaolinite ± alumino-phosphate-sulfate minerals around central cores of alunite ± kaolinite. A methodology for the discrimination of these halos using ASTER data based on the greater band depth of dickite relative to that of kaolinite is proposed that can identify areas of high-grade argillic alteration.

The mineral maps of the White Horse deposit generated from low-altitude AVIRIS data have been demonstrated to accurately portray the primary geologic features of the deposit. The 3-meter pixel size of these data is well suited for delineating most surface features of the deposit, including the fracture-controlled argillic selvages, which are typically 2–3 meters wide.

The high-altitude AVIRIS data with 17-meter pixel size are capable of delineating the central alunite zone and surrounding alunite + kaolinite transition and dickite-bearing argillic zones, the pyritic "proximal" propylitic/phyllic zone, which underlies and surrounds the argillic zones, and "distal" propylitically altered volcanic rocks containing calcite and possible chlorite. However, when compared to the map derived from the low-altitude AVIRIS data, the occurrence of dickite is overestimated at the expense of areal and intimate mixtures of kaolinite ± alunite in low abundance; thus, pixels matched to dickite had been labeled as a mineralogically mixed map unit. If the high-grade argillic alteration detected using the band-depth analysis is merged with the standard shortwave-infrared mineral mapping, the ASTER data (30-meter pixel size) are also capable of delineating most primary deposit features and zoning, but the clay-free central alunite zone (30–32 meters wide) cannot be discriminated from the surrounding alunite + kaolinite transition zone because of areal mixing effects. In addition, areal mixing of alunite, clay minerals, and dry vegetation having leaf biochemical absorptions overlapping with the primary sulfate feature of alunite resulted in an overdetection of alunite-bearing mineral assemblages at the expense of clay minerals, mainly kaolinite.

All maps are presented in a variety of digital formats, including jpeg, pdf, and ERDAS Imagine (.img). The Imagine format files are georeferenced and suitable for viewing with other geospatial data in Imagine, ArcGIS, and ENVI. The mineral and vegetation maps are attributed so that the material identified for a pixel can be determined easily in ArcMap by using the Identify tool and in Imagine by using the Inquire Cursor tool.

Introduction

High-resolution spectroscopic image data collected on October 17, 1999, by the Airborne Visible/Infrared Imaging Spectrometer (AVIRIS) sensor from a low-altitude Twin Otter turboprop platform (AVIRIS flightline metadata) were analyzed for a detailed study of the surface mineralogy of a Miocene epithermal replacement alunite deposit several kilometers north of the town of Marysvale, Utah, along the southeastern edge of the Antelope Range (Rockwell and others, 2006). Multispectral image data collected by the Advanced Spaceborne Thermal Emission and Reflection Radiometer (ASTER) sensor carried aboard the Terra satellite platform orbiting the Earth at 705-kilometer (km) altitude were analyzed to show the distribution of hydrothermal alteration throughout the Antelope Range and surrounding area. This report presents digital versions of the mineral and vegetation maps produced from the AVIRIS and ASTER data in both Portable Document Format (.pdf), ERDAS Imagine format (.img), and JPEG format (.jpg). The methodologies used to process and analyze the ASTER data are described. The PDF and JPEG format maps are useful for printing and detailed viewing through zooming. The Imagine format files are useful for integrating the maps with other geospatial data in a geographic information system (GIS) and have been fully attributed with material identification information, so that the material(s) identified in a pixel can be queried using software tools such as the Inquire Cursor Tool in Imagine and the Identify Tool in ArcMap.

Geographic and Geologic Setting of the White Horse Mine and Surrounding Area

The White Horse mine is located at 1,982 meters (m) above sea level on undulating terrain that slopes gently downward toward the Sevier River, 3 km to the west at 1,771-m elevation (fig. 1). Precipitation increases with elevation, and the Sevier River valley receives on average about 25 centimeters (cm) annually and the lower slopes of the valley as much as 30 cm (Daly and others, 1994, 1997). The high Tushar Mountains (3,710-m maximum elevation) to the west receive as much as 125 cm annually, and the Sevier Plateau to the east (3,422-m maximum elevation) as much as 90 cm. The area surrounding the mine is covered with sparse sagebrush and grasses, with piñon and juniper becoming more abundant with increased elevation and precipitation east of the mine. Figure 2 is a perspective view of the Antelope Range area that shows the location of the White Horse mine in relation to other mines and important geographic and geologic features. In figure 2, green vegetation (shown in hues of green) can be seen to increase in density with increasing elevation and rainfall.

The geologic setting of the study area is described by Rockwell and others (2006, and references therein). The geology and structure of the Antelope Range area are shown in figure 3. The area is underlain by eroded stratovolcanoes and related calc-alkaline volcanic rocks of the Bullion Canyon Volcanics (30–22 Ma, fig. 3) that intruded and covered a sequence of Paleozoic and Mesozoic sedimentary rocks. Cores of these volcanoes and several monzonite porphyry intrusions including the Hoover pluton (HP in fig. 2, Tbci in fig. 3) that have been interpreted as the solidified magma sources of some of the younger Bullion Canyon Volcanics (Rowley and others, 2002) are exposed along Marysvale Canyon (fig. 2). The Three Creeks Tuff Member (≈27 Ma) of the Bullion Canyon Volcanics exposed in the central Tushar Mountains (including Alunite Ridge) is derived from the Three Creeks caldera in the southern Pahvant Range (fig. 1). Most of the Antelope Range lies within the inferred boundary of the Monroe Peak caldera (fig. 3), which erupted near 23 Ma and produced the Osiris Tuff, which has been altered at the White Horse deposit. The central intrusion (≈23 Ma, unit Tci in fig. 3), a composite intracaldera intrusion of quartz monzonite stocks thought to

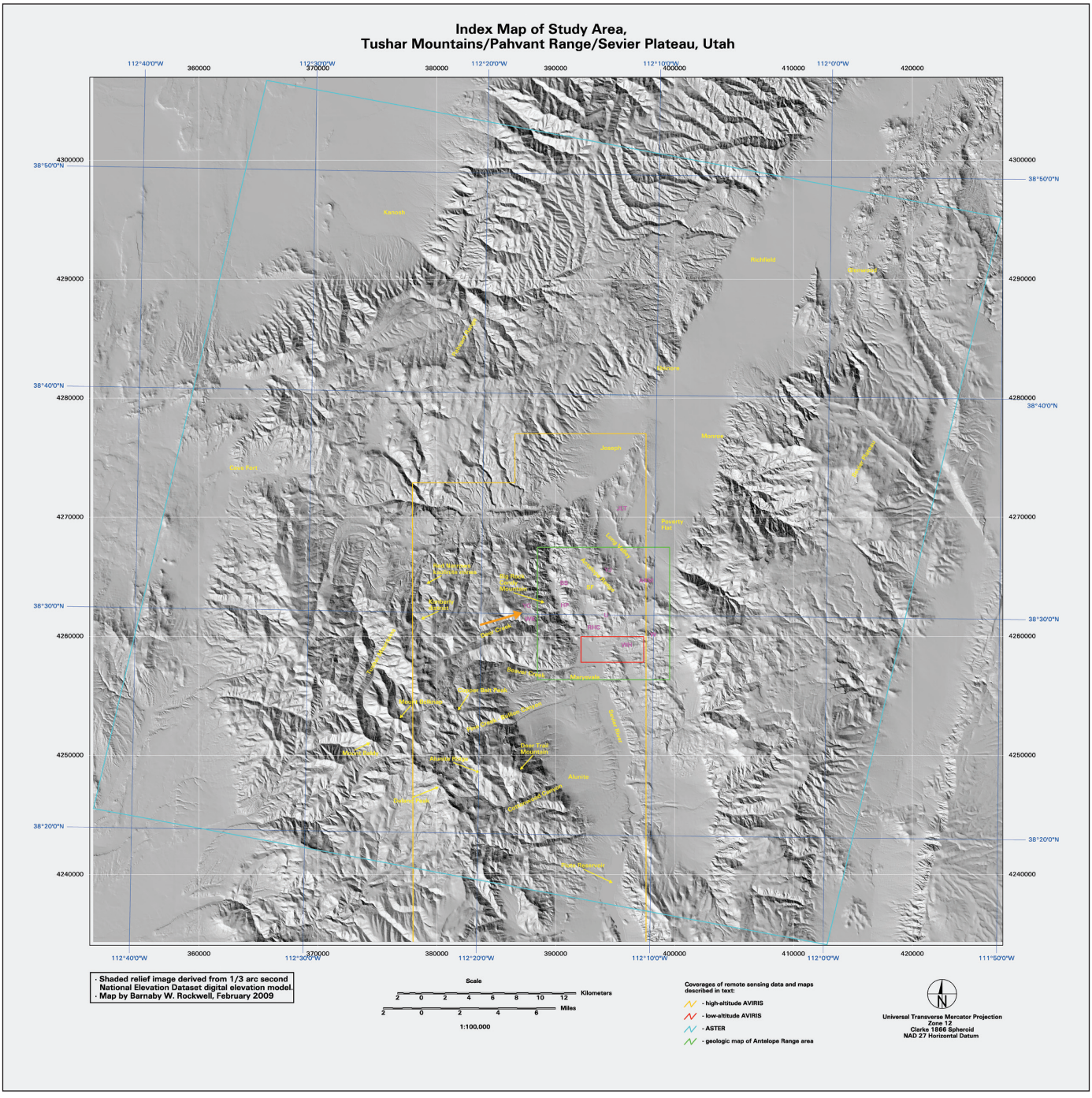


Figure 1. Index map of study area showing footprints of ASTER data (cyan), high-altitude AVIRIS data (gold), low-altitude AVIRIS data (red), and geologic map shown in figure 3 (green). The large orange arrow indicates the viewing direction of the perspective image shown in figure 2. Background is shaded relief produced from 1/3 arc second digital elevation data from the National Elevation Dataset (NED). Selected deposits, mines, and geologic features (magenta): AKM = Al Kee Mee natroalunite deposit; BS = Big Star natroalunite deposit; HP = Hoover pluton; JLT = Joe Lott Tuff Member of Mount Belknap Volcanics; RHC = Red Hills caldera; U = Jungfrau Peak and uranium mining area; W = White Hills alunite deposit; WH = White Horse alunite deposit; WK = Winkleman alunite deposit; YC = Yellow Cougar gold mine; YJ = Yellow Jacket alunite deposit. Geographic features (yellow): SF = Sage Flat. Larger image is available **HERE**. PDF version of figure is available **HERE**.

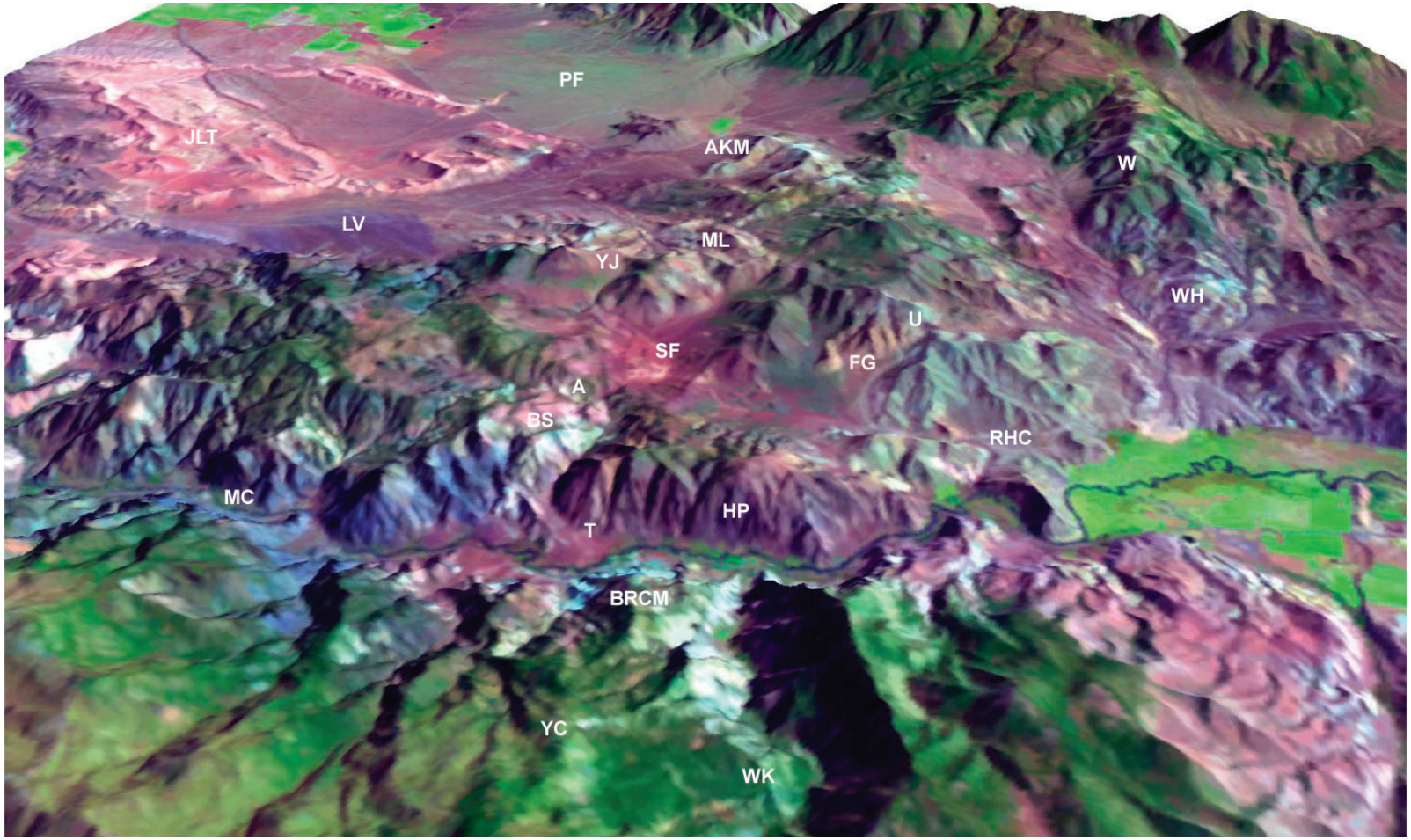


Figure 2. Perspective view of the Antelope Range area looking toward the northeast. Orange arrow in figure 1 shows direction of view. Image overlay is a color composite (741/RGB) of Landsat 7 Enhanced Thematic Mapper Plus (ETM+) data. The approximate horizontal distance between the White Horse deposit (WH) and the center of the Red Hills caldera (RHC) is 3.7 kilometers. Cultivated fields and riparian vegetation in the Sevier River flood plain at the north end of Marysvale Valley are visible in bright green at right center. Geographic features: LV = Long Valley; MC = Marysvale Canyon and Sevier River; PF = Poverty Flat; SF = Sage Flat, location of a small exposure of pyrophyllite (Rockwell and others, 2005). Geologic features: FG = Fine-grained granite (21–20 Ma, unit Tmf in fig. 3); JLT = Joe Lott Tuff Member of the Mount Belknap Volcanics, dipping to the east and northeast away from the viewer; RHC = Red Hills caldera surrounded by hematite-bearing Red Hills Tuff Member of the Mount Belknap Volcanics (unit Tmr in fig. 3). Alunite deposits: BRCM = Big Rock Candy Mountain; ML = Mary's Lamb mine in southeastern part of Yellow Jacket deposit (the "Silica Hills" of Kerr and others, 1957) adjacent to highly silicified rocks bearing dickite and local topaz (Rockwell and others, 2000); W = White Hills; WH = White Horse; WK = Winkleman; YJ = Yellow Jacket, which contains a small but rich deposit of hematite (associated with natroalunite-bearing veins and breccia fragments) exploited by the Iron Cap mine located at high levels in the Yellow Jacket deposit immediately beneath and partially within a resistant, silicified, sub-sinter cap (Callaghan, 1973; Cunningham and others, 1984a). Natroalunite deposits: AKM = Al Kee Mee; BS = Big Star. Copper, gold, and gold-silver deposits: A = Antelope (gold, silver); T = Trinity (copper), a skarn deposit developed in a faulted slice of Permian limestones immediately adjacent to the Hoover pluton; YC = Yellow Cougar (gold). U = Jungfrau Peak and uranium mining area.

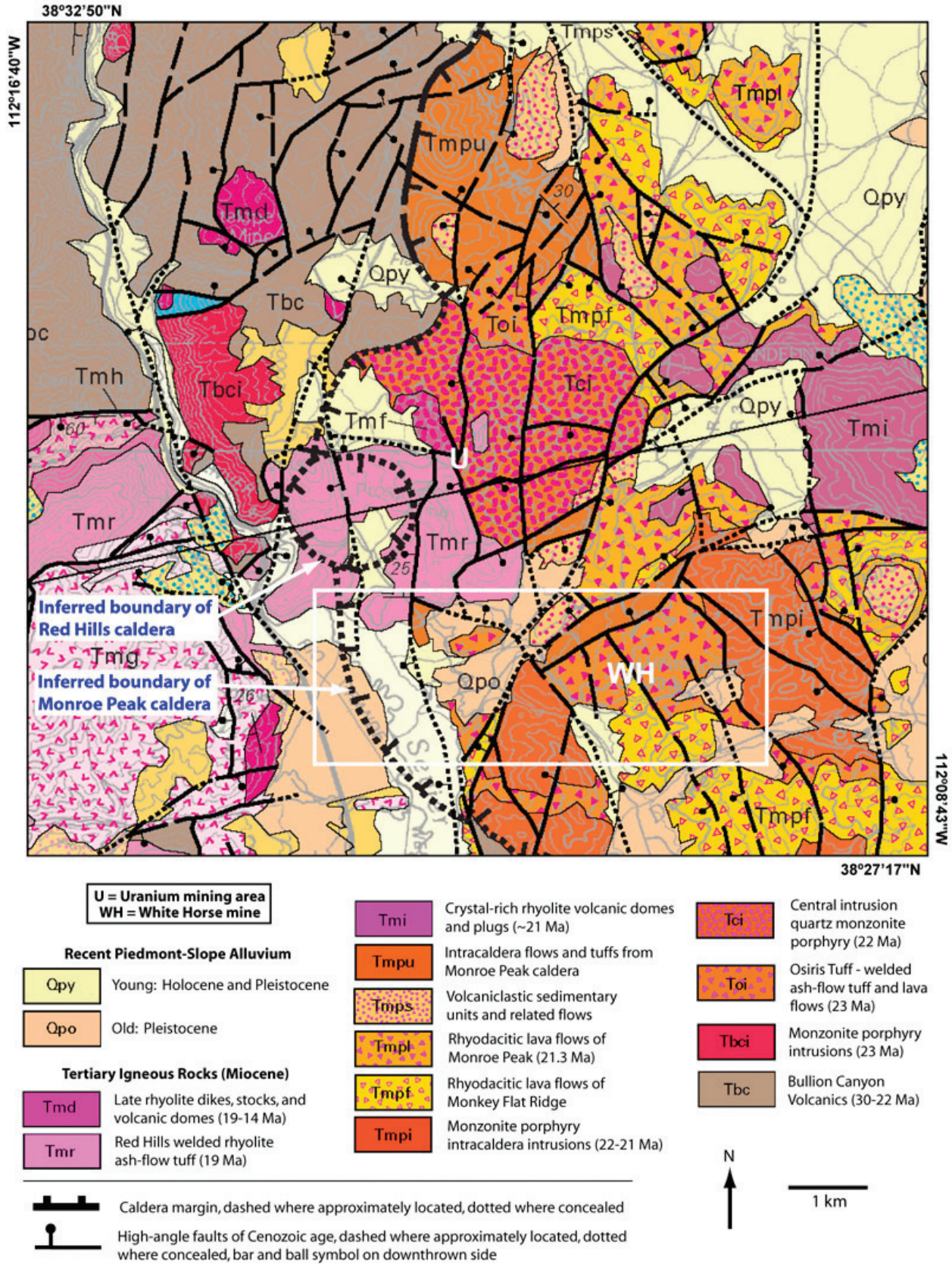


Figure 3. Geologic map of southern Antelope Range and surrounding area. The white rectangle indicates approximate coverage of 1999 low-altitude AVIRIS data over the White Horse deposit. Larger image is available **HERE**. PDF version of figure is available **HERE**. Modified from Rowley and others (2002).

be the source of hydrothermal activity that formed surrounding small deposits of copper, gold, and silver (for example, Antelope, Yellow Cougar, and Trinity, fig. 2) and replacement alunite of similar age, is centered about 1 km northeast of the uranium mining area in the Antelope Range (figs. 2 and 3). The Big John caldera also formed at or just before this time in the south-central Tushar Mountains, erupting the Delano Peak Tuff Member of the Bullion Canyon Volcanics. With the onset of tectonic extension and Basin and Range faulting around 23–22 mega-annum (Ma), volcanism changed to bimodal composition. The Mount Belknap Volcanics (21–12 Ma) are present throughout the study area and emanated from several caldera and volcano eruptive centers including the Mount Belknap (north-central Tushar Mountains) and Red Hills (fig. 2) calderas, which erupted close to 19 Ma, producing the Joe Lott and Red Hills Tuff Members, respectively. Exposed and concealed intrusions of granitic (fine-grained granite, fig. 2) to rhyolitic composition with related domes, flows, and tuffs lie along a southwest-trending belt extending from the Antelope Range to Alunite Ridge (fig. 1) with age decreasing toward the southwest. These intrusions are thought to be the source of uranium mineralization in the Antelope Range (fig. 2), polymetallic mineralization in the eastern Tushar Mountains near Copper Belt Peak (fig. 1), along Bullion Canyon, and at the Deer Trail mine, as well as the ≈14-Ma magmatic steam alunite deposits on Alunite Ridge that could be related to porphyry molybdenum mineralization (fig. 1). Basin and Range faulting accelerated between 8 and 5 Ma, initiating the formation of Marysvale Canyon by the downcutting of the Sevier River along entrenched meanders and deforming basin-fill sediments such as the Sevier River Formation (22–7 Ma). Bimodal volcanic activity in the area continued until the Pleistocene.

Mineral and Vegetation Maps Derived from AVIRIS data

The low-altitude AVIRIS data and the techniques used to analyze them are described by Rockwell and others (2006). Mineral maps produced from high-altitude AVIRIS data of the White Horse deposit, the Antelope Range, and the eastern Tushar Mountains are shown in Rockwell and others (2000, 2005). The footprints of the low- and high-altitude AVIRIS data are shown in figure 1. Both the high- and low-altitude AVIRIS data were analyzed using a modified version (Rockwell, 2002) of an expert system (Clark and others, 2003a) that quantitatively compares continuum-removed image spectra and laboratory reference spectra using least-squares curve-fitting techniques. Figure 4 shows a true-color composite image of the AVIRIS flightline covering the White Horse deposit. Areas in which ferric iron minerals are abundant on the surface appear in red to brown hues in this image. Vegetation appears in hues of green. Spectral analysis of the AVIRIS data produced a map of iron-bearing minerals and water (fig. 5) and a map of clay, sulfate, mica, carbonate, and Mg-OH minerals (fig. 6).

Eroded remnants of what could be another hydrothermal system are exposed 2 km west-northwest of the White Horse mine adjacent to the Sevier River flood plain (fig. 5). In this area, the Osiris Tuff contains abundant jarosite, local hematite, and mixtures of kaolinite and illite/muscovite (figs. 3, 5, and 6). The assemblage of jarosite, kaolinite, and illite/muscovite is indicative of the pyrite-bearing, "proximal" propylitic (or phyllic) alteration of a feeder system (Cunningham and others, 2005; Rockwell and others, 2005, 2006). The hematite may be the only remnant of the overlying advanced argillic assemblage. The lack of any residual alunite and the relatively small size of this altered area relative to other replacement alunite deposits in the Antelope Range suggest that this hydrothermal system was only weakly developed. The east-northeast elongation of the alteration suggests it was controlled primarily by faults and (or) fractures as opposed to volcanic stratigraphy or massive replacement above an upwelling fluid plume. The deposit is situated on the southern, upthrown side of a west-northwest-trending, high-angle fault that passes immediately to the north (fig. 3). The southern edge of the deposit is aligned with a northeast-southwest-trending fault mapped less than a kilometer to the east.

To examine the spatial relationships between mineralogical variations and vegetation, the AVIRIS data were analyzed to determine vegetation distribution and vigor. Vegetation identified with the AVIRIS data was classified into four broad classes based on spectral absorptions related to chlorophyll (0.67 micrometer [μm]), leaf water content (0.98 and 1.18 μm), and (or) the leaf biochemicals such as lignin and cellulose (~2.10 and 2.33 μm) that cause very strong absorptions in dry, senescing vegetation (Clark and others, 2003a, and references therein). Figure 7 shows averaged AVIRIS spectra sampled randomly from high fit × depth pixels of each class (Rockwell and others, 2005, 2006). Principal absorption features are labeled, and the pigments or biochemicals responsible for the absorptions are indicated. Prominent absorption features related to carotenoid pigments, chlorophyll, and leaf water, but very weak to nonexistent leaf biochemical features, characterize the spectrum of dense, moist, green vegetation. With increasing dryness and (or) decreasing per-pixel vegetation density (top to bottom), the chlorophyll and leaf water features are seen to decrease in depth while the leaf biochemical features increase in depth.

Figure 8 shows the distribution of the four vegetation classes in the White Horse area. The class "green, moist vegetation" represents a spectral match to the chlorophyll and leaf water features of a green lawn grass and corresponds to green grasses in the Sevier River flood plain and to piñon/juniper at higher elevations to the east of the White Horse mine. The weak/sparse green vegetation class represents a match to the chlorophyll and leaf water features of an areal mixture of soil and sparse green grasses. This class corresponds to either

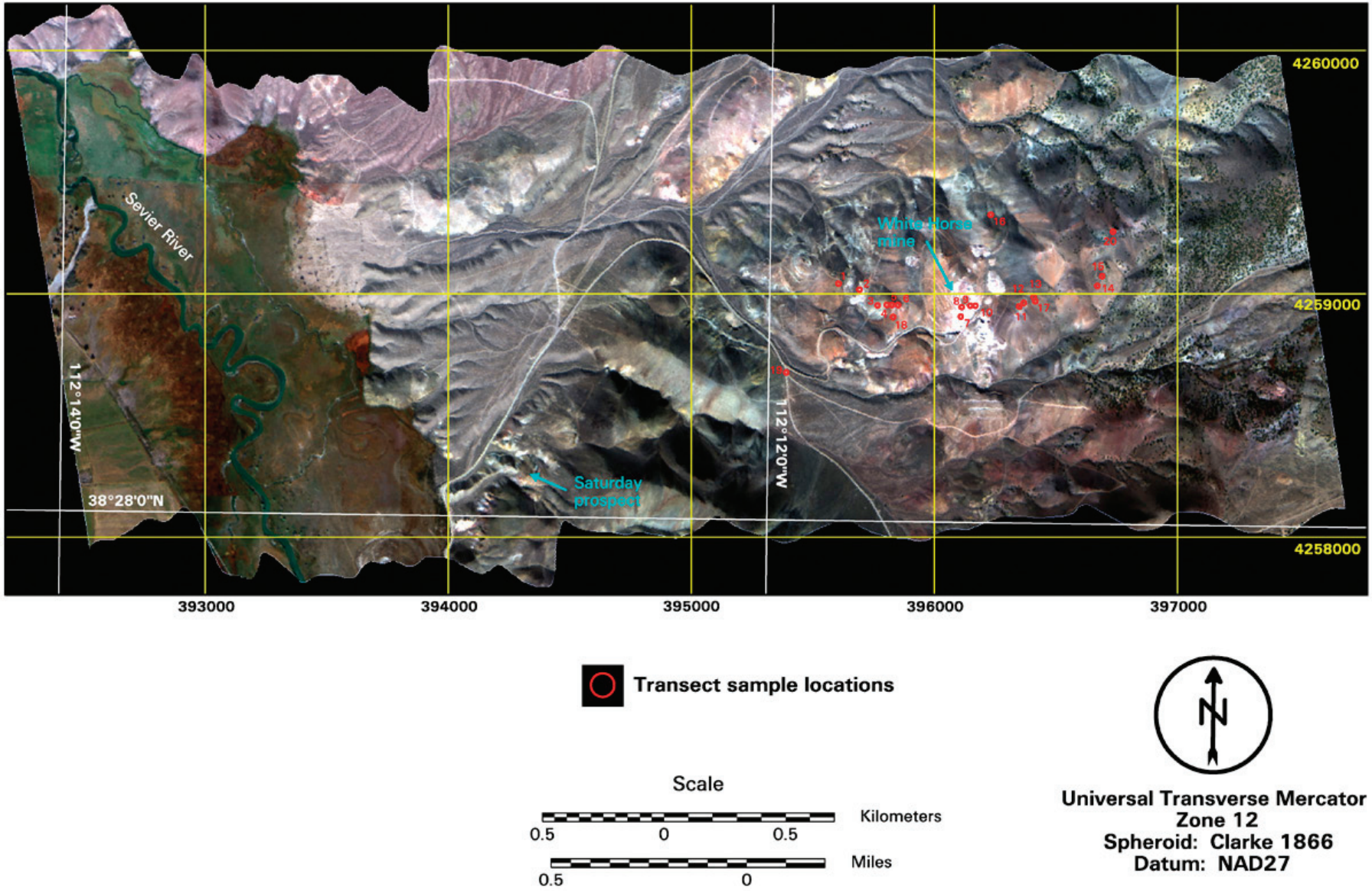


Figure 4. True-color composite of AVIRIS flightline over White Horse deposit (red = band 36, 0.682790 micrometer; green = band 19, 0.547320 micrometer; blue = band 9, 0.449060 micrometer). Mineralogy and geochemistry of the samples from the locations shown in red are described by Rockwell and others (2006). Larger image is available **HERE**. PDF version of figure is available **HERE**. ERDAS Imagine format data are available **HERE**.

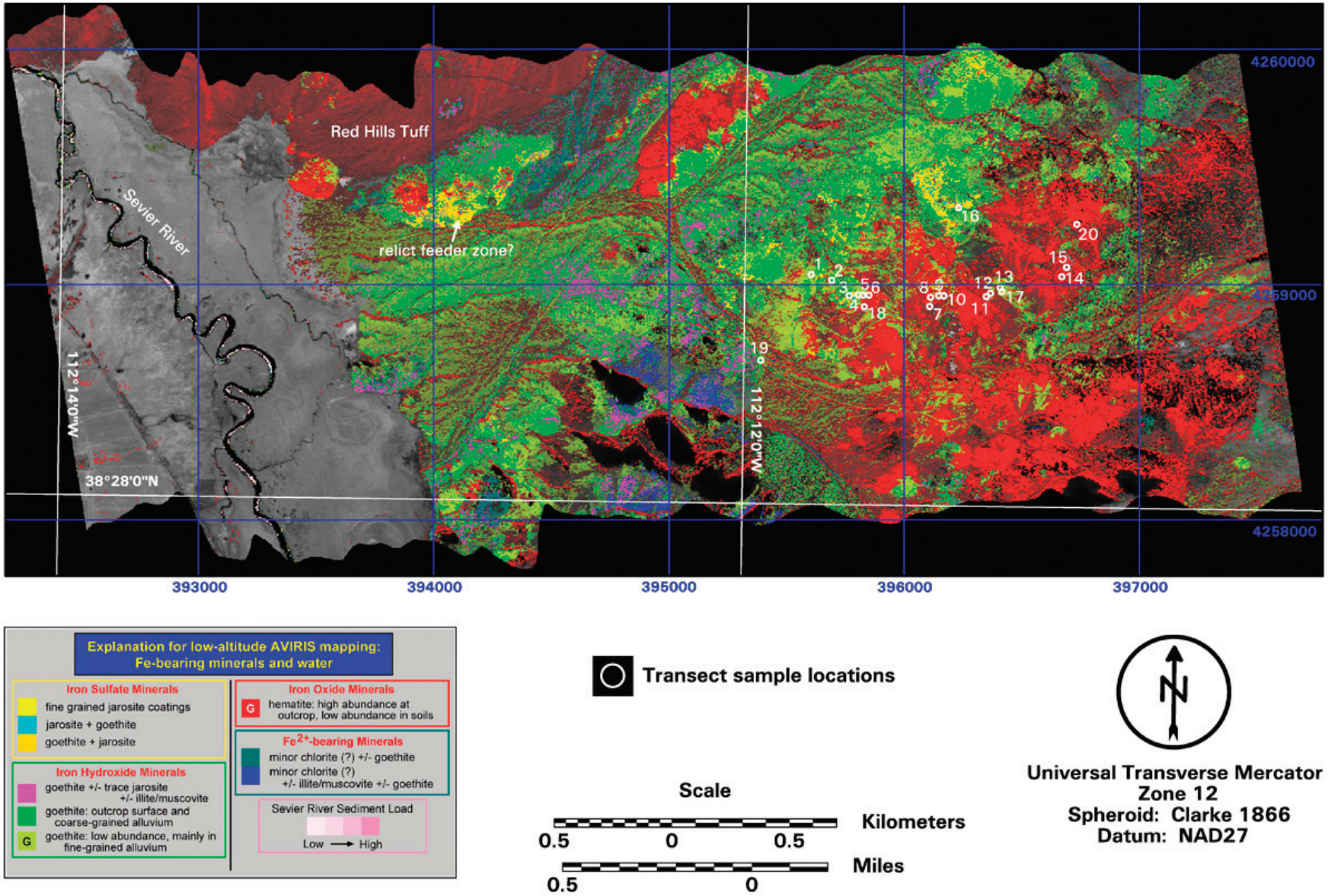


Figure 5. Map of iron-bearing minerals and water generated from AVIRIS data in the 0.35–1.35-micrometer region. G = gradational stretch applied. Materials displayed with a gradational stretch show bright colors where the identification had high fit × depth (least-squares fit of reference to image spectrum times depth of diagnostic absorption feature), and darker color brightness with successively lower fit × depth values (Rockwell and others, 2005, 2006). Sample collection locations are indicated with white circles. "Red Hills Tuff" indicates exposures of the Red Hills Tuff Member of the Mount Belknap Volcanics. Larger image is available **HERE**. PDF version of figure is available **HERE**. A similar map covering this area that was produced from high-altitude 1998 AVIRIS data is available **HERE** (Rockwell and others, 2005). ERDAS Imagine format data are available **HERE** with material identifications attributed for use in a GIS.

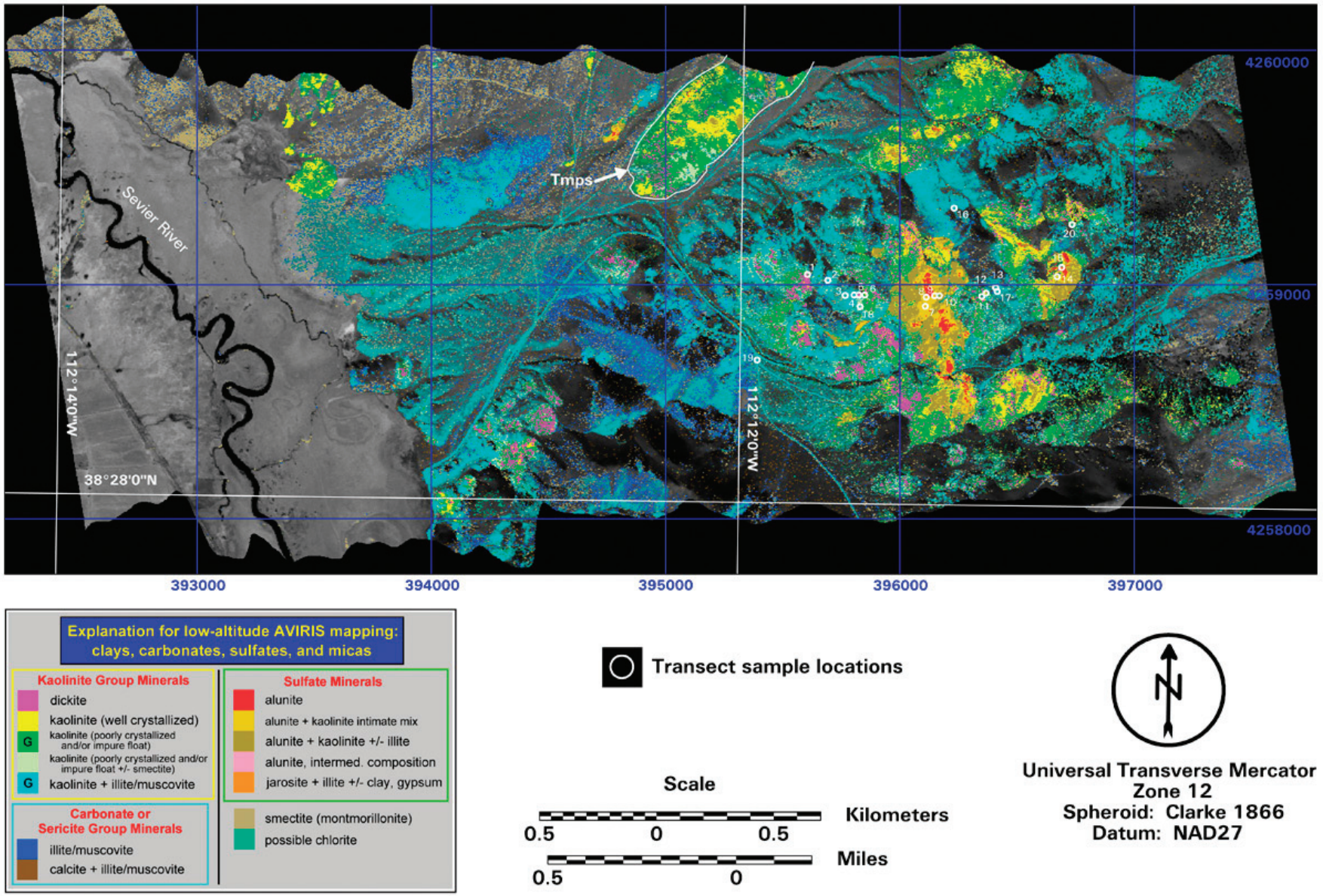


Figure 6. Map of clay, sulfate, mica, carbonate, and Mg-OH minerals generated from AVIRIS data in the 1.45–2.50-micrometer region. "Tmps" indicates a Tertiary volcaniclastic sedimentary unit (fig. 3) that preferentially alters to kaolinite with local dickite and alunite (Rockwell and others, 2006). G = gradational stretch applied. Sample collection locations are indicated with white circles. Larger image is available **HERE**. PDF version of figure is available **HERE**. A similar map covering this area that was produced from high-altitude 1998 AVIRIS data is available **HERE** (Rockwell and others, 2005). ERDAS Imagine format data are available **HERE** with material identifications attributed for use in a GIS.

sparse green grasses in the flood plain or to areal mixtures of piñon/juniper, soil, and (or) sparse dry grasses that occur mainly on the more shaded north-facing slopes of the hills and drainages surrounding the White Horse deposit. These areas are underlain by unaltered to weakly altered rocks and soils. The dry, green vegetation class represents a match to chlorophyll, leaf water, and leaf biochemical features of an areal mix of dry and green vegetation, and the dry, nonphotosynthetic vegetation (DNPV) class matches only the leaf biochemical absorption features in a reference spectrum of dry, long grasses. The dry vegetation classes map primarily in the flood plain. The dry, green vegetation class occurs around pixels of DNPV and represents a transition between very dry, senesced DNPV grasses and moister green grasses.

A comparison of the AVIRIS-derived mineral (figs. 5 and 6) and vegetation maps (fig. 8) shows that little to no vegetation other than very sparse grasses and sage grow on areas underlain by altered rocks, or by the Red Hills Tuff Member along the northwestern edge of the AVIRIS flightline. Most of the grasses were completely senesced at the time of the October AVIRIS overflight. Very little vegetation of any kind typically grows on the altered, pyritic rocks of the propylitic feeder zones of the hydrothermal systems in the Antelope Range area. In addition to mapping surface mineralogy, imaging spectroscopy provides a means for the rapid characterization of vegetation at prospects, mines, or mill sites and can reveal geobotanical relationships for enhanced understanding of local lithology and alteration. Also, it can be used to identify vegetation that has been stressed due the presence of metals or acid soil conditions.

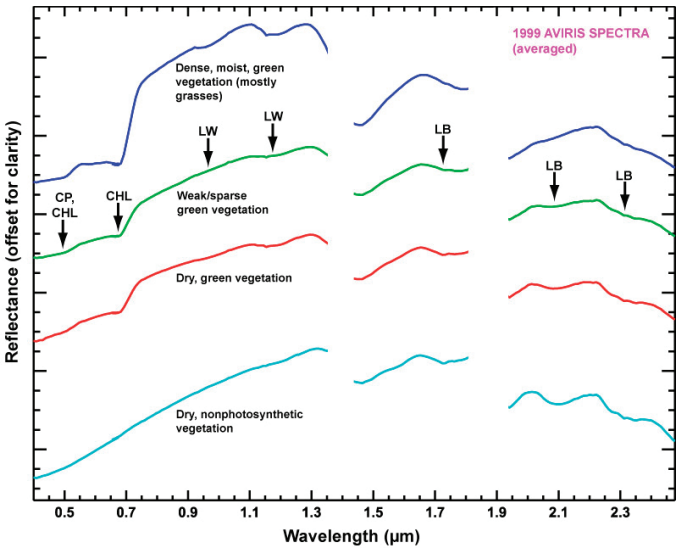


Figure 7. Averaged AVIRIS spectra of vegetation classes. Spectra were sampled randomly from high fit × depth pixels of each mapped class. Chlorophyll content decreases and dryness increases from top to bottom, expressed by the decrease in band depth of the chlorophyll absorption band at 0.68 µm (micrometer) and the increase in depth of the leaf biochemical bands at 1.73 µm, 2.09–2.14 µm and 2.28–2.34 µm. Principal absorption features are marked with plant components responsible for the absorption. CP = carotenoid pigments. CHL = chlorophyll. LW = leaf water. LB = leaf biochemicals (for example, lignin, cellulose). µm, micrometers. PDF version of figure is available **HERE**.

Processing and Analysis of ASTER Data

ASTER Level 1B (L1B, Registered Radiance At Sensor) data acquired on June 12, 2002, were analyzed to obtain a synoptic, regional overview of exposed hydrothermal alteration in the area surrounding Marysvale. Analysis of ASTER data is an efficient and cost-effective method of generating regional alteration maps, which traditionally have been compiled through extensive field work and sampling (Cunningham and others, 1984b).

ASTER scenes can be acquired with either nadir or off-nadir viewing geometries. When scenes are acquired with pointing angles greater than 6 degrees from nadir, horizontal positional errors in the ephemeris data can be severe (up to 400 m) (Rockwell and Hofstra, 2008). The pointing angle of the Marysvale ASTER scene is –8.5 degrees (ASTER scene metadata). In such significantly off-nadir scenes, and in areas with significant topographic relief, orthocorrection is important when integrating ASTER-derived mapping products with other geospatial data. For nonorthocorrected Level 1B data that has geometric coefficients applied, ephemeris-based orthocorrection is impossible. However, projective transforms using ground control points and a digital elevation model (DEM) with spatial resolutions similar to that of the ASTER data (for example, USGS 1/3 arc second DEM data with 10-m resolution from National Elevation Dataset) are very useful for geometric modeling of the ASTER data and can yield very low positional error. Such a transform was applied to the Marysvale ASTER scene.

ASTER data from the visible (VIS), near-infrared (NIR), and shortwave infrared (SWIR) spectral regions (table 1) were converted to radiance units (λ/m2/sr/µm) through multiplication by gain settings in the metadata after subtracting minimum, nonzero digital number (DN) values from the SWIR data on a band-by-band basis to reduce effects of stray light referred to as “crosstalk” (Iwasaki and Tonooka, 2005; Iwasaki and Oyama, 2005). The SWIR data were resampled to 15-m spatial resolution to match the ground instantaneous field of view (GIFOV) of the VIS and NIR data (table 1).

To calibrate the ASTER radiance data to unitless relative reflectance format in preparation for comparison with reference reflectance spectra, the radiance spectrum of each ASTER pixel was divided by the average radiance spectrum of a calibration site covered by the ASTER data in which no prominent absorption features are present (“Flat Field”

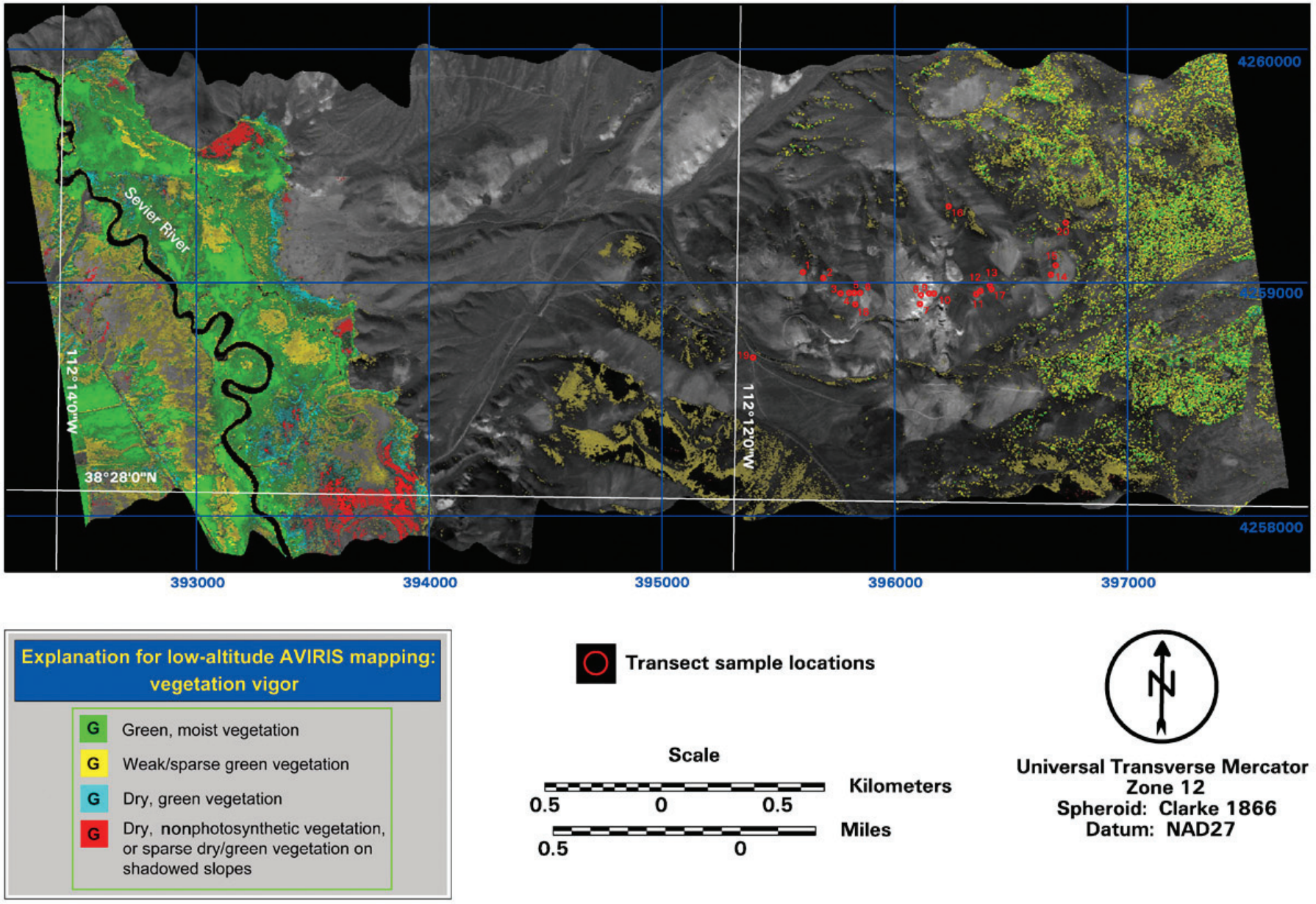


Figure 8. Map of vegetation vigor and dryness generated from AVIRIS data. G = gradational stretch applied. Sample collection locations are indicated with red circles. Larger image is available **HERE**. PDF version of figure is available **HERE**. ERDAS Imagine format data are available **HERE** with material identifications attributed for use in a GIS.

Table 1. Measured spectral performance of ASTER VIS, NIR, and SWIR bands.

[N, nadir viewing geometry; µm, micrometer; m, meter. Data from ASTER User's Guide (Earth Remote Sensing Data Analysis Center, 2005)]

ASTER Band	Central wavelength (µm)	Bandwidth (µm)	GIFOV (ground pixel size)
1	0.556	0.09	15 m
2	0.661	0.06	15 m
3 (N)	0.807	0.10	15 m
4	1.656	0.092	30 m
5	2.167	0.035	30 m
6	2.208	0.040	30 m
7	2.266	0.047	30 m
8	2.336	0.070	30 m
9	2.400	0.068	30 m

method). Although this calibration technique introduces error in the overall shape, or hull, of the data by assuming a flat calibration-site spectrum when few surfaces are truly spectrally flat, the technique is ideal for use in frontier areas for which no field spectral data of a calibration site are available. In general, empirical line calibrations (for example, Rockwell and others, 2002, 2005, 2006) using reflectance data of a field surface as a reference source yield more accurate results. However, if continuum removal techniques are used to remove the spectral hull prior to data analysis, shape errors in the hull caused by Flat Field calibration have not been found to significantly affect accurate material identification.

The ASTER reflectance data were analyzed for mineral and vegetation content using an approach based on the principles of imaging spectroscopy that identifies spectral absorption features in the ASTER spectra and is similar to that used for the AVIRIS data in this study. This approach was originally developed for analysis of high spectral resolution, or spectroscopic, data (Clark and others, 2003a) and was adapted by the author for analysis of full scenes of ASTER multispectral data. The semiautomated approach involves continuum removal and least-squares curve fitting of ASTER spectra to selected laboratory reference spectra over spectral intervals characterized by diagnostic absorption features in the reference spectra. Reference spectra (Clark and others, 2003b) were convolved to ASTER spectral resolution (table 1) prior to analysis. Reference materials and material mixtures were selected for analysis of the ASTER data if they occur abundantly on the Earth's surface in a wide variety of geologic and climatic environments and have absorption features that are diagnostic and unique at ASTER spectral resolution. Care was taken to include mineral assemblages that occur within hydrothermal alteration systems so that patterns of mineralogic zonation could be identified and mapped. This analysis methodology is currently being applied to an ASTER-based regional mineral resource and geoenvironmental assessment of the Central Colorado Mineral Belt (Church and others, 2008) and to a regional mineral resource assessment in southwestern Utah (Rockwell and Hofstra, 2009).

Mineral and Vegetation Maps Derived from ASTER Data

False-Color Composite Image—Vegetation, Snow, and Surface Albedo

Figure 9 shows a false-color composite image produced from edge-enhanced ASTER radiance data (bands 431/RGB). Green vegetation is displayed in hues of green, and the brightness of the green color is proportional to chlorophyll content. Irrigated agricultural vegetation is visible in bright green, moist riparian vegetation and deciduous regrowth are shown in bright to medium green, and forest vegetation in dark green. Unvegetated, high albedo areas, which in the high Tushar Mountains and Antelope Range often represent altered volcanic rocks, are shown in white to light blue colors. In the Tushar Mountains, the bright areas correspond with volcanic rocks of the Mount Belknap and Big John calderas that have undergone regional propylitic (sericite and chlorite, Callaghan, 1973) to low-grade argillic alteration. In the Antelope Range, the bright areas mainly correspond to pyritic, "proximal propylitic" (or phyllic) alteration in the feeder zones of the replacement alunite deposits, or locally correspond to mined, argillically altered areas of these deposits. Unaltered to propylitically altered ("distal" type with calcite, chlorite and (or) epidote) igneous rocks with low albedo are visible in dark blue, especially within Marysvale Canyon along the western edge of the Antelope Range (fig. 2). Snow is visible in shades of cyan because of intense infrared absorption and is limited to the high Tushar Mountains.

Visible and Near-Infrared Mapping—Iron Minerals

Reference spectra of iron-bearing minerals, vegetation, and water used for analysis of the ASTER data with key absorption features labeled, and representative examples of ASTER spectra of pixels identified as specific materials based on spectral similarity with the reference spectra, are shown in figure 10. Figure 11 shows a map these materials produced from the ASTER data. Note that some of the identified materials are depicted using a gradational stretch to show variation in the fit × depth of the diagnostic absorption feature(s) used for analysis of that material (see map explanation and fig. 5). Fit × depth is proportional to both the least-squares fit of ASTER spectra to laboratory reference spectra and the depth of the diagnostic absorption feature(s) in the ASTER spectra. Low feature depths may indicate lower abundance of the mineral type in the pixel, given a constant grain size. For green vegetation, low feature depths (darker shades of green) may indicate decreased areal abundance and (or) chlorophyll content. Pixels identified as dry vegetation (shown in yellow in fig. 11) may also include carbonate, chlorite, and (or) epidote in low abundance.

The most important mineralogical feature of the map (fig. 11) is the discrimination of reddish soils and rocks bearing hematite and goethite, shown in orange hues on the map,

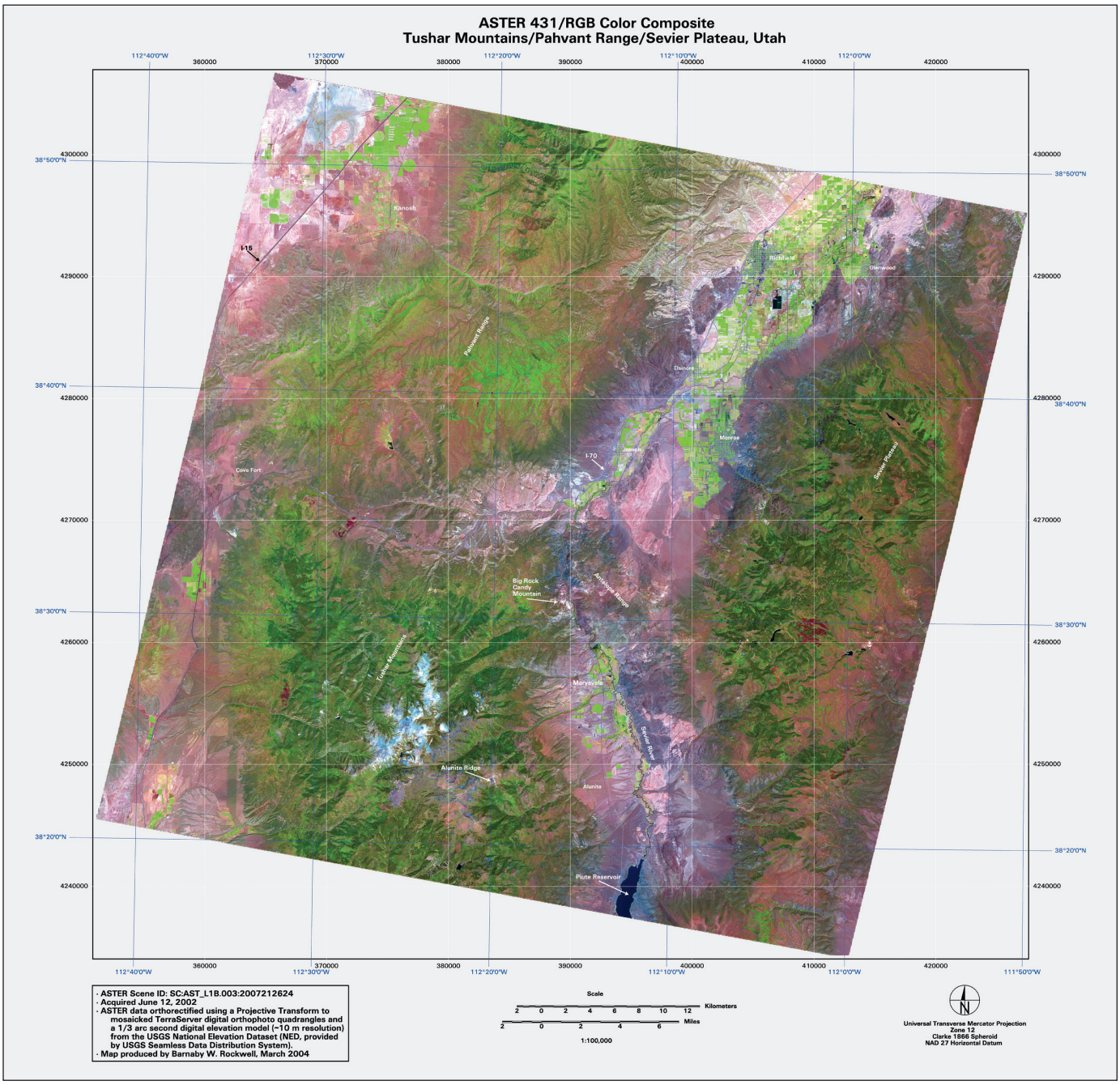


Figure 9. Map showing ASTER 431/RGB false-color composite image of the Marysvale region. Larger image is available **HERE**. PDF version of figure is available **HERE**. Edge-enhanced radiance data of bands 1–4, 6, and 8 are available **HERE** in ERDAS Imagine format.

from high concentrations of ferric iron sulfates, hydroxides, and local oxides (shown in hues of red on map) that have more yellowish to orange color in outcrop and correspond mainly to hydrothermally altered rock, including phyllic alteration that is overprinted by supergene alteration caused by the weathering of pyrite. The reddish rocks and soils bearing hematite and (or) goethite shown in orange are characterized by a broad, convex-up hull in the VIS–NIR with deep absorption in the shortest ASTER wavelengths caused by iron absorption features in the ultraviolet and are spectrally similar to nanohematite at ASTER spectral resolution (fig. 10). The spectra of these rocks are not characterized by significant electronic crystal field absorptions near 1.0 µm typical of ferric iron minerals (Rockwell, 2004, and references therein). Rocks with these VIS–NIR spectral characteristics include the upper and middle red members of the Flagstaff Formation (Paleocene and Eocene; reddish-brown, interbedded calcareous mudstone, siltstone, and sandstone), the Crazy Hollow Formation (Oligocene; brownish-orange to brownish-red fine-grained sandstone, siltstone, and mudstone), both well-exposed west and north of Richfield (Hintze and others, 2003), the Red Hills Tuff Member of the Mount Belknap

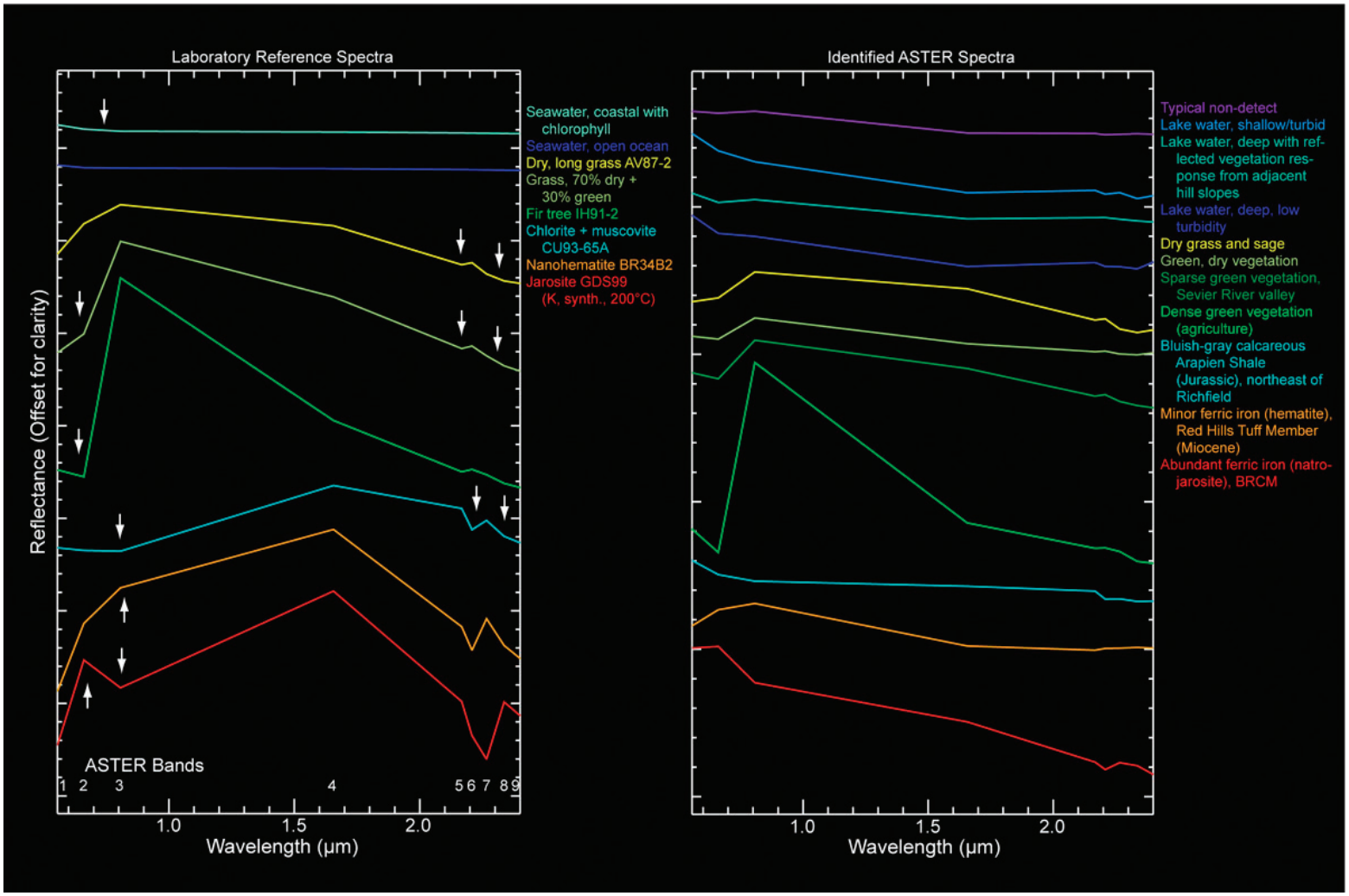


Figure 10. Plot of selected convolved laboratory spectra of iron-bearing minerals, vegetation, and water (on left) used as references for analysis of ASTER data. The mapped results of the analysis are shown in figure 11. Except for chlorite + muscovite, dry/green grass, and dry grass, most spectral features analyzed for these materials are in the VIS and NIR spectral regions. Reference spectra of additional minerals and materials (for example, copiapite, melting snow, and cummingtonite for generic ferrous iron) included in the VIS–NIR image analysis are not shown. Representative ASTER image spectra of pixels identified as specific materials based on spectral similarity with the reference spectra are shown at right with sampling locations, surface features, or lithologic unit. An ASTER spectrum selected from a pixel in which no materials were detected is shown in purple at top right. White arrows indicate diagnostic absorption features used in analysis. Note that emission features are also analyzed (upward-pointing arrows). Color of the spectra match the colors assigned to the identified materials in figure 11. BRCM = Big Rock Candy Mountain. Larger image is available **HERE**. PDF version of figure is available **HERE**.

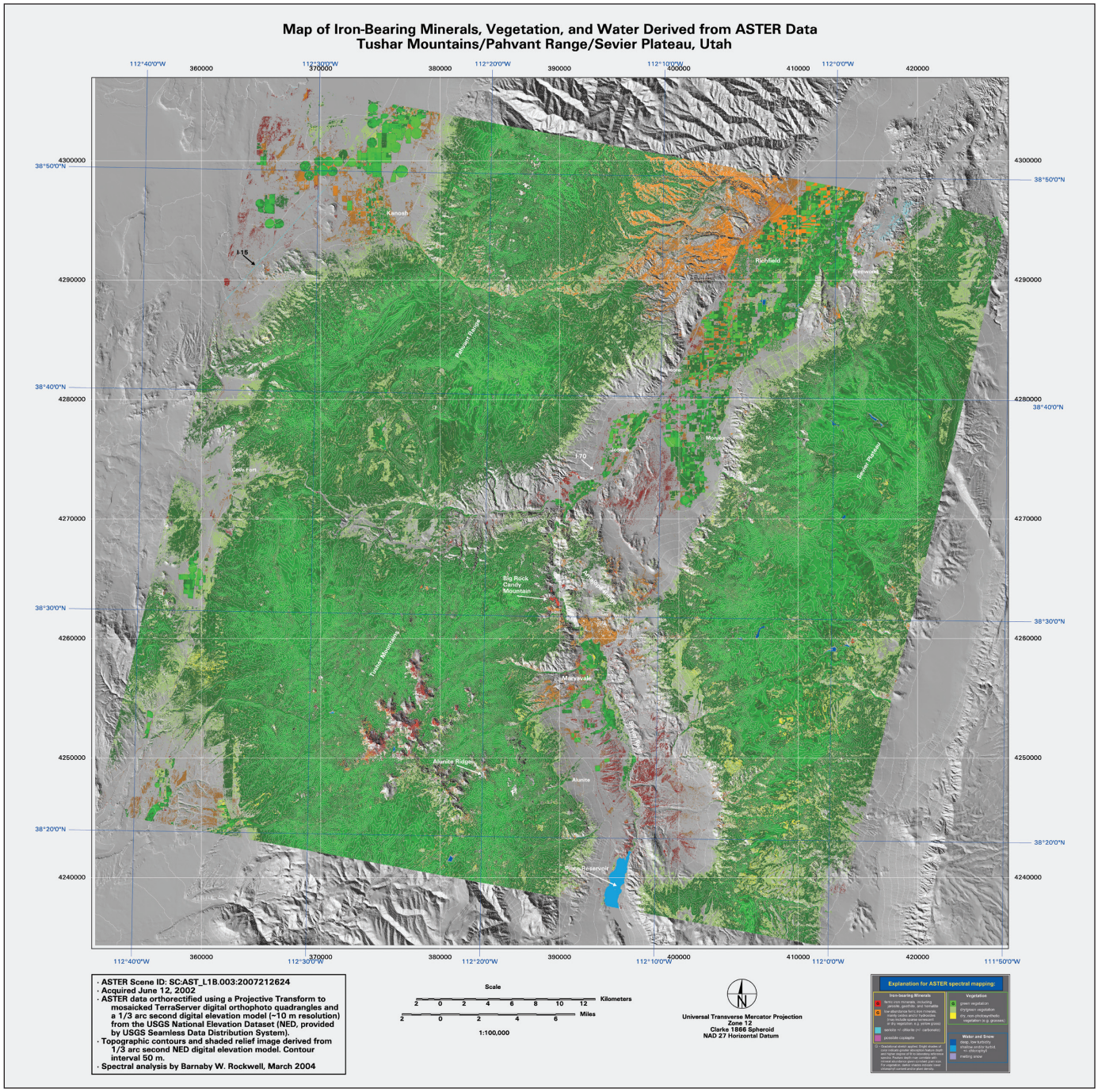


Figure 11. Map of iron-bearing minerals, vegetation, and water derived from spectral analysis of ASTER data. Larger image is available **HERE**. PDF version of figure is available **HERE**. ERDAS Imagine format data are available **HERE** with material identifications attributed for use in a GIS.

Volcanics (Miocene, figs. 2 and 3) several kilometers north of Marysvale, and locally in altered rocks in the Antelope Range and Tushar Mountains, including Alunite Ridge and the Red Narrows kaolinite deposits on the northern slopes of the Tushar Mountains 3 km north of the Kimberly mining district (Rockwell and others, 2005). The basal section of the middle white member of the Flagstaff Formation contains reddish sandstone layers interbedded with limestone and gypsiferous mudstone (Hintze and others, 2003) that give the member similar spectral characteristics but with lesser fit × depth values (a more subdued convex shape) and thus is shown in slightly darker shades of orange in figure 11. Northeast of Richfield, alluvial soils in fallow fields derived from the red rocks of the Flagstaff and Crazy Hollow Formations show high fit × depth values (brightest orange) similar to those of the sedimentary rocks from which they are derived. South of Richfield, the ferric iron content of the soils in fallow fields decreases as the bedrock sources of the soils switch to

unaltered volcanic rocks. Ferric iron with low to moderate fit × depth values (dark orange in fig. 11) was detected in goethitic (Rockwell and others, 2005) tailings deposits from the Old Deer Trail mine 2.2 km northwest of the old Alunite townsite (site of a loading and processing facility for alunite mined from Alunite Ridge in the middle 20th century and the current site of the mill for the Deer Trail mine). As the base metal mantos under Deer Trail Mountain are highly pyritic (Beaty and others, 1986), it is likely that most pyrite in the tailings has oxidized, and most of the resultant jarosite has weathered to goethite.

Rocks with abundant ferric iron minerals (shown in red in fig. 11) that were a spectral match to jarosite in the VIS–NIR (fig. 10) have significant ferric iron absorptions near 1.0 µm (ASTER band 3) and can be considered to have higher concentrations of ferric iron than the areas shown in orange and discussed herein that were a spectral match to nanohematite. Areas with these spectral features include intense argillic and advanced argillic alteration in the Antelope Range, Tushar Mountains, and Sevier Plateau, supergene weathering of phyllic alteration at Big Rock Candy Mountain and the nearby Big Star alunite deposit, and alluvial fan deposits along the west bank of the Sevier River containing abundant alunite and kaolinite derived from the erosion of the 14 Ma alteration on Alunite Ridge and Deer Trail Mountain (Rockwell and others, 2005). Altered rocks with similar spectral features were also identified locally in basin fill of the Sevier River Formation (Miocene and Pliocene) west and northwest of Marysvale, and in intracaldera fill of the Mount Belknap caldera in the high Tushar Mountains that has undergone regional propylitic (Callaghan, 1973) and local argillic alteration. Concentrations of ferric iron having absorption near ASTER band 3 and high fit × depth values (bright to medium red in fig. 11) are important targets for field sampling of hydrothermally altered and potentially mineralized rocks.

Several pixels with VIS–NIR–SWIR spectral characteristics of the ferric iron sulfate-hydrate mineral copiapite (Clark and others, 2003b, ***http://pubs.usgs.gov/of/2003/ofr-03-395/PLOTS/M/copiapite_gds21.2201.gif***) were identified on the flanks of Big Rock Candy Mountain (shown in magenta in fig. 11). Copiapite, in addition to alunogen and epsomite, occur in this highly pyritic phyllic alteration zone as precipitates from acidic fluids in drainage channels after rainfall (Cunningham and others, 2005). Although melting snow (Clark and others, 2003b, ***http://pubs.usgs.gov/of/2003/ofr-03-395/PLOTS/L/melting_snow_1-16.9366.gif***) is used as a reference material, several pixels of melting snow in the high Tushar Mountains were misidentified as copiapite because they have absorptions of unknown origin near 1.0 µm like those of copiapite. Both melting snow and copiapite show marked decreases in reflectance from the NIR to the SWIR; thus, some confusion between these materials can be expected when mapping at ASTER spectral resolution. Most thick melting snow was correctly identified (light purple in fig. 11).

Vegetation

Green vegetation with pronounced chlorophyll absorption at ASTER band 2 (table 1) was detected at low to moderate elevations in the Tushar Mountains, Pahvant Range, and Sevier Plateau. Abundant and moist green vegetation with the highest chlorophyll content per pixel (brightest green in fig. 11) was detected in agricultural fields and riparian environments including spring-fed drainages in the mountains. Green vegetation on north-facing slopes is typically characterized by greater chlorophyll abundance per pixel (deeper chlorophyll absorptions shown in brighter tones of green in fig. 11) than green vegetation on more exposed southern slopes. Dry and green vegetation with both chlorophyll and lignin/cellulose SWIR absorptions were detected mainly on surfaces with low relief, both along the fringes of the green vegetation in the mountainous areas and in high plateaus above treeline. The dry and (or) green vegetation detected at lower elevations (and concomitant lower annual precipitation) surrounding the mountainous areas represents transitional vegetation communities between upland pine, aspen, and (or) maple forest with significant chlorophyll and relatively dry lowland vegetation including piñon, juniper, and sage. The mapping of such variations in vegetation dryness and greenness suggest that ASTER data may provide an efficient alternative to spectroscopic data for studies of burn severity after forest and rangeland fires for which the analysis of AVIRIS data has been proven to be useful (Kokaly and others, 2006).

Shortwave-Infrared Mapping and Detector "Scratch"

Selected reference spectra used in the analysis of the ASTER SWIR data are shown in figure 12, along with representative ASTER spectra of pixels identified as the reference materials based on spectral similarity. Figure 13 shows a map these materials produced from the ASTER data, a subset of which was published by Rockwell and others (2006). An important feature of figure 13 is the region of erroneous mineral detections indicated by the magenta rectangle that is oriented parallel to the satellite path approximately 20 km from the western edge of the ASTER scene (one-third of the image swath). This area of corrupted SWIR spectral response is present in all ASTER scenes and is related to a physical defect (detector "scratch") in the SWIR detectors (Iwasaki and Oyama, 2005; Iwasaki and Tonooka, 2005). The SWIR data in this image region are characterized by a false and uneven reduction in the response of band 5 (table 1), resulting in erroneous detections of materials having absorptions in those wavelengths, including alunite, pyrophyllite, and kaolinite. Kaolinite in this region may appear spectrally similar to alunite and may be falsely identified as such. A polygon shapefile indicating the region affected by the SWIR detector "scratch" is provided with this report. Although difficult to recognize in figure 13, another parallel

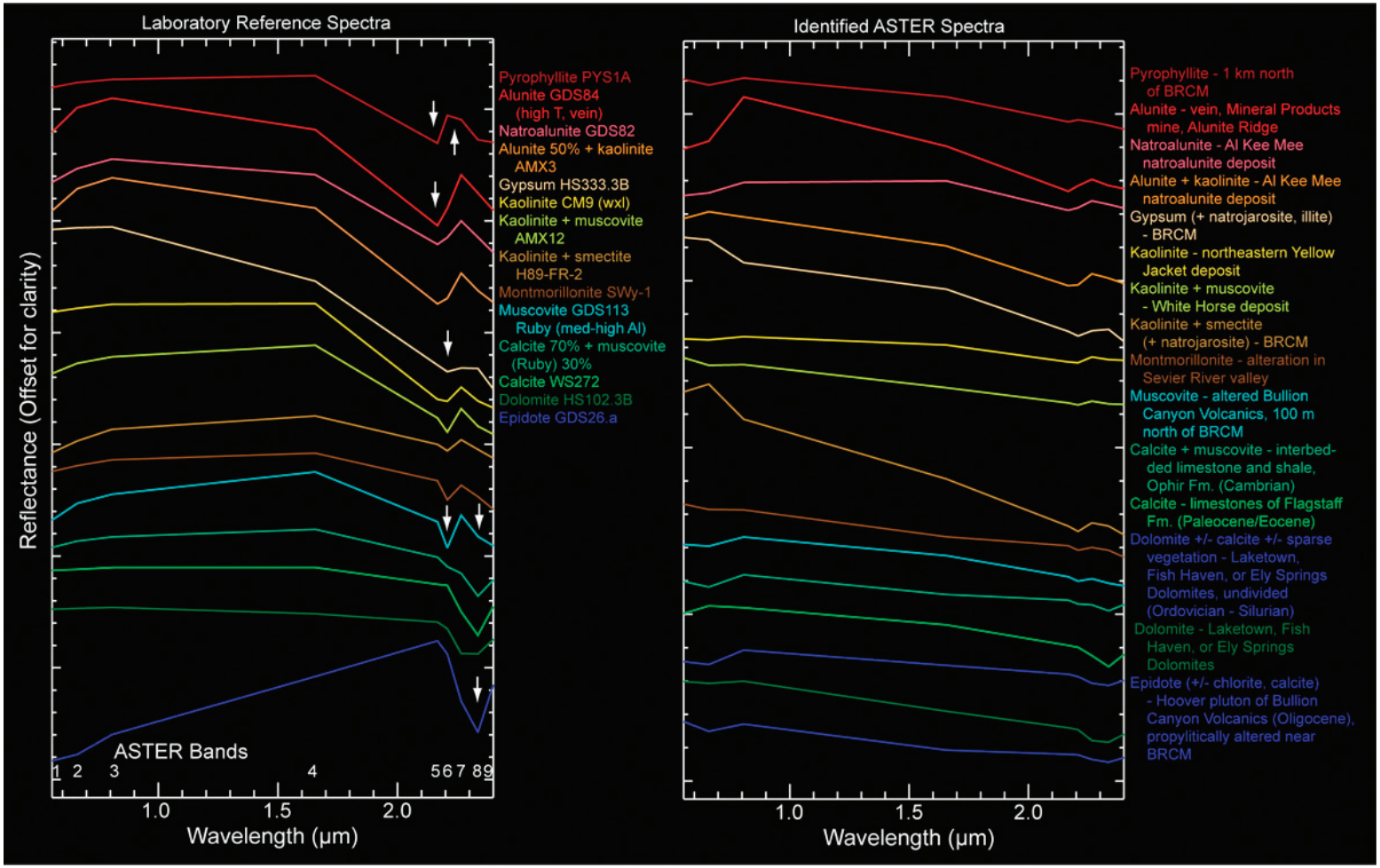


Figure 12. Plot of selected convolved laboratory spectra of clay, sulfate, mica, carbonate, and sorosilicate (epidote) minerals and mineral mixtures having diagnostic SWIR absorption features (on left) used as references for analysis of ASTER data. The mapped results of the analysis are shown in figure 13. Reference spectra of additional minerals (for example, chlorite, chalcedony, and jarosite) included in the SWIR image analysis are not shown. Representative ASTER image spectra of pixels identified as specific materials based on spectral similarity with the reference spectra are shown at right with their sampling locations, surface features, or lithologic unit. White arrows indicate selected diagnostic absorption features used in analysis. Note that emission features are also analyzed (upward-pointing arrow). Color of the spectra match the colors assigned to the identified materials in figure 13. BRCM = Big Rock Candy Mountain. wxl = well-crystallized. Larger image is available **HERE**. PDF version of figure is available **HERE**.

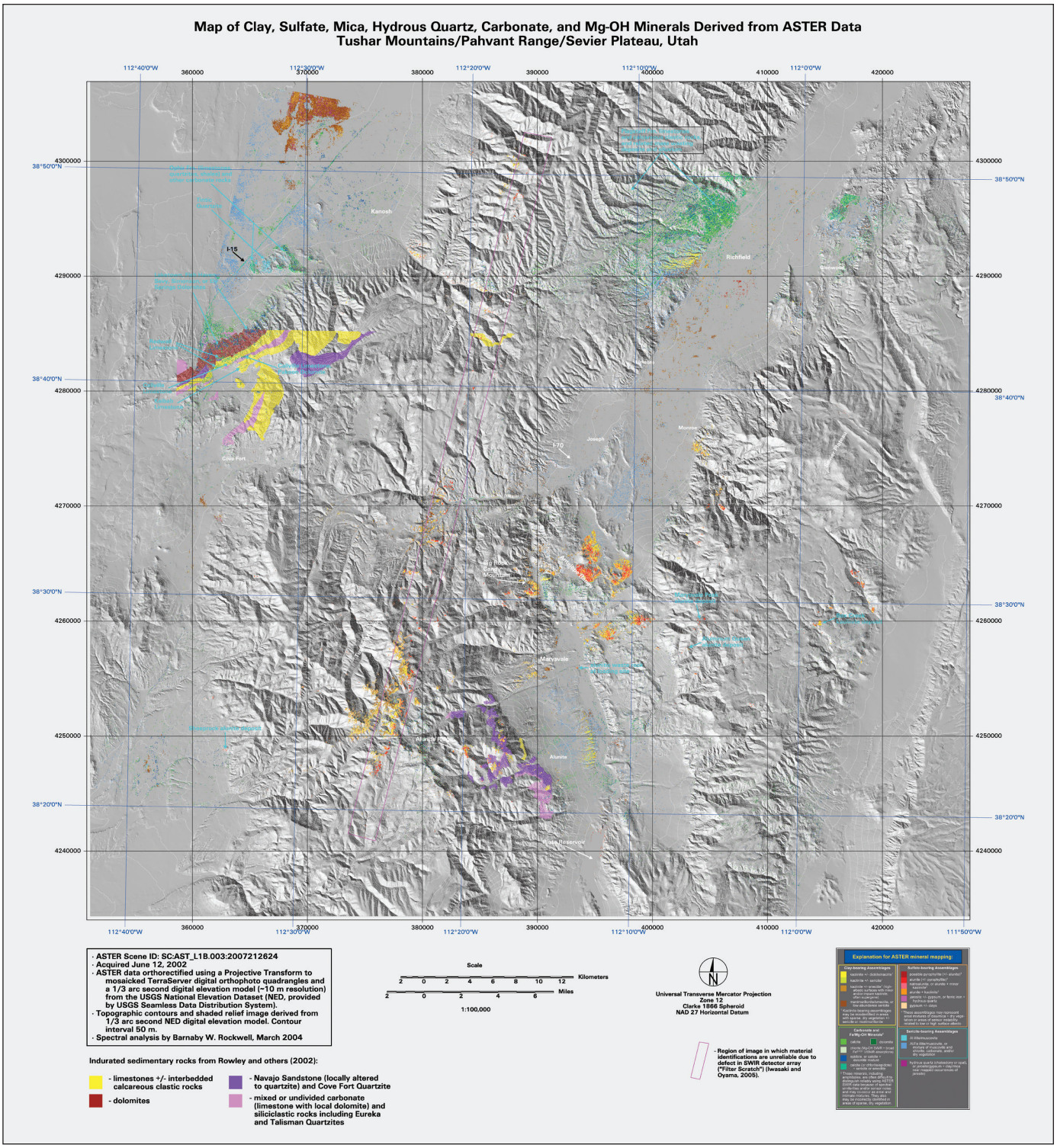


Figure 13. Map of clay, sulfate, mica, hydrous quartz, carbonate, and Mg-OH minerals derived from spectral analysis of ASTER shortwave infrared (SWIR) data. Larger image is available **HERE**. PDF version of figure is available **HERE**. ERDAS Imagine format data are available **HERE** with material identifications attributed for use in a GIS. Indurated sedimentary rocks from Rowley and others (2002) are also shown as colored polygons.

but less pronounced defect exists immediately to the east of the region affected by the primary detector scratch. The SWIR data affected by this secondary defect are characterized by false reductions in the response of band 7, resulting in erroneous detections of carbonate minerals, chlorite, and epidote. Calcite in this region may appear spectrally similar to dolomite or epidote. Jarosite and hydrous quartz (for example, chalcedony) also have diagnostic absorptions near band 7 and thus may also be incorrectly identified. For example, jarosite detected using the ASTER SWIR data (magenta in fig. 13) within argillized Joe Lott Tuff Member of the Mount Belknap Volcanics (unit Tmj of Rowley and others, 2002) on Copper Belt Peak (fig. 1) 10.4 km west of the town of Marysvale above the Copper Belt mine lies within the region affected by the secondary defect and is most likely incorrect. However, abundant ferric iron minerals were detected in that area by using the ASTER VIS–NIR data (red in fig. 11), and goethite (+ kaolinite + sericite, surrounding hematite + smectite on peak 10962 closest to the mine) was detected using high-altitude AVIRIS data (figs. 48 and 49 in Rockwell and others, 2005).

Advanced Argillic Alteration and Areal Mixing

In figure 13, advanced argillic alteration associated with the primarily steam-heated alunite deposits surrounding 23–21 Ma intrusive rocks are clearly visible in the Antelope Range north of the town of Marysvale. Alunite related to higher-temperature magmatic steam deposits was detected in the east-central Tushar Mountains, including along Alunite Ridge, at the small L & N deposit 1 km to the west, and at the Close In colluvial alunite deposit in the Sevier River valley. Alunite and kaolinite were also detected at the foot of the mountains along Gold Gulch 2.5 km south-southeast of the Alunite townsite within Quaternary basin fill (unit QTs of Rowley and others, 2002) adjacent to outcrops of volcanic rocks erupted from both the Mount Belknap and Monroe Peak calderas. The identified alunite and kaolinite in these deposits correlate well with the distributions of these and related minerals mapped by AVIRIS data (fig. 6 and figs. 49, 51, and 53 of Rockwell and others, 2005). Alunite was also detected at the Sheeprock alunite deposit on the southwestern edge of the Tushar Mountains and in several locations on the Sevier Plateau, including southeast of Monroe (mainly 1.2 km south and 2 km south-southeast of the Monroe hot spring), the Marysvale Peak and Aluminum Queen alunite deposits within the Monroe Peak caldera, and on the eastern side of the plateau along Greenwich Creek 5 km northeast of the Box Creek kaolinite deposit (Callaghan, 1973). Primarily kaolinite was identified at the Box Creek deposit.

Because of the 30-m GIFOV of the ASTER SWIR data, areal mixing of materials has an increased effect on spectral shape than in remote sensing data with smaller GIFOV such as AVIRIS data. For example, areal mixtures of kaolinite (Al-OH vibrational absorptions at bands 5 and 6) and dry vegetation (lignin/cellulose absorptions at bands 5 and 8, fig. 7 and table 1) can result in a spectrum similar to that of alunite characterized by deep absorption at band 5 and moderate absorption at band 6. Such spectral mixing results in a general overdetection of alunite throughout the ASTER scene, especially where abundant dry vegetation is present adjacent to argillically altered rocks.

Natroalunite was identified using the ASTER SWIR data at the Big Star and Al Kee Mee natroalunite deposits, and in wall-rock alteration surrounding the alunite veins on Alunite Ridge (figs. 12 and 13). The natroalunite (+ quartz + kaolinite + pyrite ± dickite) on Alunite Ridge was also identified using AVIRIS data (Rockwell and others, 2005) and confirmed in the laboratory (Rockwell, 2002). However, pixels with spectral features similar to that of natroalunite at ASTER spectral resolution were also identified at the White Horse deposit, where none was found using AVIRIS data (fig. 6) and field sampling. Mixtures of alunite with minor kaolinite have SWIR spectral features similar to those of natroalunite at ASTER spectral resolution, and thus pixels matched to natroalunite using ASTER data were classified on the map explanation of figure 13 either as natroalunite or mixtures of alunite and minor kaolinite. ASTER SWIR data do not have sufficient spectral resolution to accurately discriminate natroalunite from mixtures of alunite and kaolinite, but pixels matched to natroalunite can be considered to be transitional in alunite content between pure alunite and mixtures of alunite with major kaolinite (fig. 12), which can be used to identify zones of maximum hydrothermal fluid conductivity, acidity, and temperature.

The replacement alunite deposits in the Antelope Range are capped by titanium-bearing, hydrofractured, subsinter silica consisting of opal and chalcedony (Rockwell and others, 2006, and references therein). These silica caps have been mostly eroded away and are best exposed at the uppermost levels of the Yellow Jacket deposit and in one boulder at the White Horse deposit. Because of the small size of the remnant caps and the presence of grasses and sage, only six pixels of hydrous quartz (spectral match to chalcedony) were identified using AVIRIS data with 17-m GIFOV in the Antelope Range, in colluvial blocks located in the central Yellow Jacket deposit (Rockwell and others, 2005). No significant, field-verified hydrous quartz associated with alunite deposits was detected in the study area using the ASTER SWIR data, although several pixels were identified in colluvium derived from altered Navajo Sandstone (Jurassic, unit Jn of Rowley and others, 2002) on the east face of Deer Trail Mountain, on Big Rock Candy Mountain, and within argillically altered rocks 6.3 km southeast of Monroe.

Phyllic Alteration and Pyrophyllite

Where the Sevier River has exposed the phyllic (or "proximal propylitic") alteration underlying the alunite at Big Rock Candy Mountain (BRCM) along Marysvale Canyon (fig. 2), the ASTER data analysis identified kaolinite + smectite, gypsum, and local kaolinite + sericite and smectite (montmorillonite) (figs. 12 and 13). These assemblages were confirmed through field sampling (Rockwell and others, 2005; Cunningham and

others, 2005) and are typical of the supergene weathering of pyritic rocks, in this case altered volcanic rocks bearing hypogene pyrite, illite, and local pyrophyllite. Similar phyllic alteration with a supergene overprint is also present in the lower parts of the nearby Big Star deposit along the east bank of the Sevier River and on the north flank of the White Horse deposit (Rockwell and others, 2006). Several pixels of pyrophyllite were detected one kilometer north of BRCM that have been verified though field checking and AVIRIS data analysis (Rockwell and others, 2005, 2006; Cunningham and others, 2005). The accurate identification of pyrophyllite and its differentiation from alunite are difficult using ASTER SWIR data because of the low spectral and spatial resolution of the ASTER data and because of the typically small exposures in which pyrophyllite occurs. Pixels with SWIR spectral characteristics similar to pyrophyllite were also identified in the Sevier Valley several kilometers southeast of Richfield. It is unlikely that these identifications of pyrophyllite are correct. They most likely represent an areal mixture of more common clay minerals and dry vegetation. Two areas with kaolinite, smectite, kaolinite + smectite, and several pixels of alunite and alunite + kaolinite were also identified in this area, although not at the same locations as the pixels with spectral features similar to pyrophyllite. These areas have not been field checked but are most likely clay minerals in alluvium derived from the Crazy Hollow Formation exposed on the flanks of the Pahvant Range west of Richfield. Areal mixtures of alunite and dry vegetation may result in spectra resembling that of pyrophyllite, as the dry vegetation will increase spectral response in band 6. Areal mixtures of alunite, lichen, and (or) other dry vegetation produced AVIRIS spectra similar to mixtures of alunite + pyrophyllite in the Silica Hills located in the southern portion of the Yellow Jacket deposit (fig. 2, Rockwell and others, 2005). Detections of pyrophyllite in the upper Silica Hills using the ASTER data may also have been influenced by such mixing effects. However, quartz-topaz-dickite assemblages in this area (Rockwell and others, 2000), in addition to natroalunite-natrojarosite-dickite-kaolinite assemblages found in the lower, southwestern part of the Silica Hills adjacent to Sage Flat (figs. 1 and 2, Rockwell and others, 2005) may indicate that the alunite in this area is magmatic hydrothermal in origin, at least in part, as it appears to be at the White Horse deposit (Rockwell and others, 2006). In epithermal environments with magmatic hydrothermal alunite such as the Goldfield mining district in Nevada (Rockwell, 2000) and Tintic mining district in Utah (Rockwell and others, 2005), pyrophyllite and alunite (and pyrite) can co-occur intimately; thus, some of the pyrophyllite in the Silica Hills may be accurate. Calcite and epidote ("distal propylitic" assemblage) were identified 1 km east of the BRCM deposit within quartz monzonites of the Hoover pluton (figs. 1 and 2; 23 Ma, Cunningham and others, 1984a, and references therein) that were propylitically altered by the Miocene hydrothermal systems active in the vicinity of BRCM. These minerals were also identified there by using AVIRIS data (Rockwell and others, 2000, 2005). Calcite and epidote ± sericite were also identified within potentially propylitically altered "Potassium-rich mafic volcanic rocks" (Miocene, unit Tpm of Rowley and others, 2002) 8 km southeast of the town of Marysvale.

Mineral assemblages similar to those at BRCM previously described were detected in mine waste and exposed bedrock near Sulphurdale, 4.6 km south of Cove Fort (fig. 13). Sulphurdale is the site of significant acid hydrothermal alteration, geothermal wells, and a large sulfur deposit that produced all of the country's native sulfur in 1893 (Callaghan, 1973). Abundant ferric iron minerals were detected there by using the VIS–NIR data (red in fig. 11), and jarosite, gypsum, and smectite were detected using the SWIR data, in addition to several pixels of alunite surrounded by kaolinite + smectite, although the area has not been field checked.

Carbonate

Between Kanosh and Cove Fort in the northwest quadrant of the ASTER scene, calcite (bright green in figs. 12 and 13) was identified in areas underlain by the Ophir Formation (mixed limestones, quartzites, and shales) and the Redwall, Callville, and Kaibab Limestones (Rowley and others, 2002; Hintze and others, 2003). Dolomite (dark green in figs. 12 and 13) and mixtures of dolomite and calcite and (or) dry vegetation (blue in figs. 12 and 13) were identified within the Laketown, Fish Haven, Sevy, Simonson, Ely Springs, and Pakoon Dolomites. Significant calcite was also identified within limestones and other calcareous rocks of the Flagstaff (middle white member) and Green River Formations west of Richfield, and related alluvium, colluvium, and mass-wasting deposits (Hintze and others, 2003). Comparison of the mineral identifications from the ASTER data and the mapped extent of the lithologic units from Rowley and others (2002), also shown in figure 13, illustrates how vegetation cover (fig. 11) obscures most of the calcite and dolomite in these carbonate units. Calcite was also identified in Quaternary hot spring travertine deposits (Hintze and others, 2003) 8 km northwest of Kanosh. North and west of the travertine, large areas of smectite and kaolinite + smectite with local hydrous silica (possibly opal and (or) chalcedony derived from hot springs) were mapped in Holocene alluvium.

Epidote

Figure 12 shows that spectral matching to the reference spectrum of epidote (blue at left) resulted in identifications of both epidote and mixtures of dolomite ± calcite ± dry vegetation (both blue at right and in fig. 13). This result can be expected, as the SWIR spectral response of epidote is very similar to that of a calcite + dolomite mixture. The mineral mapping results should be compared to geologic maps to determine the lithology and origin of carbonate, chlorite, epidote, and amphibole identified using ASTER data, as these minerals are similar in SWIR response at ASTER spectral resolution. In addition, these minerals often occur as intimate and areal mixtures with each other, especially given the large GIFOV of ASTER SWIR data. The differentiation of these minerals is further complicated by areal mixing with dry vegetation which is also characterized by absorption at ASTER bands 7 and 8 (figs. 7 and 10).

Sericites

The analysis of the ASTER SWIR data for sericite (white potassium mica) was performed using four reference spectra of muscovites having a range of cation substitutions between aluminum and iron/magnesium (Clark and others, 2003a). Increases in iron or magnesium in the muscovite structure will result in a shift of the primary Al-OH vibrational absorption to slightly longer wavelengths. In figure 13, pixels shown in cyan that are labeled "Al illite/muscovite" are spectral matches to either muscovite GDS113 Ruby (medium to high aluminum), muscovite CU91–250A (medium aluminum), or muscovite CU93–1 (low aluminum) (Clark and others, 2003b). Pixels labeled "Al/Fe illite/muscovite" in figure 13 (shown in medium blue) were a spectral match to an iron-rich muscovite (GDS116 Tanzania) and have spectra characterized by a flatter spectral response between bands 6 and 9 than aluminum sericite. Pixels matched to iron-rich muscovite (and other low-aluminum muscovite reference spectra) may represent chlorite + muscovite mixtures, especially where they correspond with pixels matched to a reference spectrum of chlorite + muscovite (fig. 10) from the VIS–NIR data analysis. This spectral confusion has also been recognized with AVIRIS data (Rockwell and others, 2005).

Spectrally pure sericite occurs in both altered and unaltered sedimentary and volcanic units. In the replacement alunite deposits of the Antelope Range, aluminum-rich sericite (cyan in fig. 13) occurs at deep levels in the Miocene hydrothermal systems distal to the phyllic (or "proximal propylitic") alteration within weakly altered volcanic rocks including the Bullion Canyon Volcanics adjacent to the BRCM and Big Star deposits (fig. 12) and locally in the Osiris Tuff surrounding the White Horse and Yellow Jacket deposits. Similar sericite was identified in the high Tushar Mountains within regionally propylitized and locally argillically altered Bullion Canyon Volcanics and along the west bank of the Sevier River within Quaternary basin fill (unit QTs of Rowley and others, 2002) derived from the altered rocks on Alunite Ridge and Deer Trail Mountain (Rockwell and others, 2005). Aluminum sericite along with kaolinite and kaolinite + sericite were identified in the Crazy Hollow Formation west of Richfield and in related alluvial and colluvial deposits (Hintze and others, 2003). Aluminum/iron sericite was identified in bentonitic siltstones, claystones, and sandstones of the Aurora Formation (40–38 Ma, unit Tau of Hintze and others, 2003) immediately to the south. Calcite and calcite + sericite were identified in thin- to medium-bedded limestone units of the Aurora Formation. Twelve kilometers east-northeast of Richfield, aluminum/iron sericite (with local smectite or low-abundance sericite without a mica absorption at ASTER band 8) was also identified in the Twelvemile Canyon Member of the Arapien Shale (Jurassic, unit Jatc of Williams and Hackman, 1971) which includes brick-red shales, bluish-gray and red gypsiferous shales, and bluish-gray calcareous shales with interbedded limestones. This sericite generally corresponds with pixels matched to chlorite + muscovite in the VIS–NIR data analysis (cyan in figs. 10 and 11), which most likely represent bluish-gray shales with sericite and VIS–NIR absorptions similar to the iron-related absorptions of chlorite. Calcareous Arapien shales and (or) limestone units are clearly differentiated by calcite and calcite + sericite identified using the ASTER SWIR data, and red shales are indicated by minor ferric iron (orange in fig. 11) identified using the ASTER VIS–NIR data. Calcite, epidote, and calcite + sericite were identified in undifferentiated latite and basaltic andesite flows (unit Tla of Williams and Hackman, 1971) in contact with the Arapien Shale in this area, indicating possible propylitic alteration.

Argillic Alteration in Quartz Arenites

As quartzites and quartz arenites are brittle and have little to no natural acid-buffering capacity, they fracture easily and are excellent hosts for fracture-controlled hydrothermal alteration. As these rocks are erosion resistant, they are typically well exposed and are thus ideal targets for remote-sensing-based mineral mapping. Therefore, such rocks may serve as important surface indicators of concealed mineral deposits in sedimentary and metamorphic terranes. Quartzites and undivided sedimentary units that include quartzites and other siliciclastic rocks in the Marysvale area are shown in figure 13. Abundant aluminum sericite was identified within an exposure of Tintic Quartzite (Cambrian) 9–10 km west-southwest of Kanosh. This sericite is most likely metamorphosed detrital muscovite in the groundmass of the quartzite. In the Tintic mining district of central Utah, the Tintic Quartzite was found to host argillic alteration including hematite + pyrophyllite, dickite, kaolinite, kaolinite + sericite, and local alunite (Rockwell and others, 2005). Kaolinite with possible local alunite was identified in Navajo Sandstone (Hintze and others, 2003) 5.5 km southeast of Kanosh along the western foot of the Pahvant Range. In the vicinity of Alunite Ridge and Deer Trail Mountain in the Tushar Mountains, the Navajo Sandstone is locally altered to quartzite and has been found to host significant argillic alteration related to the magmatic steam alunite deposits and base- and precious-metal manto deposits at the Deer Trail mine dated at 14 Ma (Rockwell and others, 2005, and references therein). Dickite was identified in Navajo Sandstone by using AVIRIS data on the upper north-northeast and south-southwest flanks of Deer Trail Mountain, and well-crystallized dickite in the groundmass of quartzite in Navajo Sandstone sampled from colluvium along the northeastern base of Deer Trail Mountain was confirmed in the laboratory. These altered rocks were also identified using the ASTER SWIR data (fig. 13). Alunite identified within the Navajo in this area has not been field verified and may represent areal mixtures of clay minerals with dry vegetation, at least in part. Vein alunite similar to that on Alunite Ridge is known to have formed above the present-day summit of Deer Trail Mountain (and the dickite in the Navajo) because of vein alunite in landslide blocks derived from the altered upper parts of the mountain found at the Close In alunite deposit in Marysvale Valley. Sericite ± kaolinite were identified in relatively weakly altered Navajo Sandstone in this area, especially where well exposed on south-facing slopes, including mainly colluvial deposits on the southwest and southeast flanks of Deer Trail Mountain and along Gold Gulch 5 km to the southeast.

Kandite Clay Differentiation

The kandite clay minerals dickite ± kaolinite may occur with quartz in fracture-controlled selvages in a variety of epithermal ore deposit types, often on the periphery of advanced argillic lithocaps (Rockwell and others, 2006, and references therein). These argillic selvages were formed by hydrothermal fluids with high silica activities and may be mineralized with base and precious metals. The dickite-bearing selvages (± alumino phosphate-sulfate minerals) usually occur distal to the halo of intimately mixed kaolinite + alunite (fig. 6) that surrounds replacement alunite deposits in the Antelope Range (Rockwell and others, 2000, 2005; Cunningham and others, 2005). As the kandite group minerals have diagnostic and complex doublet Al-OH absorption features in the SWIR that vary in shape with crystallinity (Crowley and Vergo, 1988; Pontual and others, 1997; Clark and others, 2003b), they are readily identifiable by using spectroscopic sensors such as AVIRIS and are thus important targets for remote-sensing-based mineral mapping. Figure 6 shows that dickite, well-crystallized kaolinite, and poorly crystallized and (or) impure kaolinite were differentiated based on spectral shape at the White Horse deposit using AVIRIS data. However, reflectance spectroscopy of the selvages from the White Horse mine indicate that dickite and kaolinite are often intimately mixed (Rockwell and others, 2006), and areal mixing of the two minerals will thus present difficulties in the remote discrimination of the minerals, especially with the large GIFOV of ASTER SWIR data.

A recent study used ASTER SWIR data to differentiate between kandite minerals in an epithermal deposit (Ducart and others, 2006). As dickite and kaolinite have similar SWIR spectral shapes at ASTER spectral resolution (fig. 14), dickite is not normally included by the author as a reference in the analysis of ASTER SWIR data, and pixels matched to a reference spectrum of well-crystallized kaolinite (fig. 10) are labeled "kaolinite ± dickite/nacrite" in the map explanation (fig. 13). To demonstrate that spectral shape alone is insufficient to accurately discriminate dickite from kaolinite, dickite was added as a reference spectrum for the analysis of the ASTER SWIR data. Figure 15 shows the results of this analysis. Based on comparison with geologic maps and results from analyses of AVIRIS and laboratory data (Rockwell and others, 2005), the differentiation of dickite and kaolinite shown in figure 15 is spurious and inconsistent. For example, pixels matched to the dickite reference spectrum occur in (1) sedimentary rocks (mainly the Crazy Hollow Formation) west of Richfield where no dickite is expected; (2) in the weathered phyllic alteration on the flanks of BRCM where no dickite is found; (3) in volcaniclastic sedimentary rocks (unit Tmps of Rowley and others, 2002) that have been found to alter preferentially to kaolinite rather than dickite (fig. 6 and Rockwell and others, 2006) 1 km northwest of the White Horse mine and in the northeastern part of the Yellow Jacket alunite deposit; and (4) in basin fill of the Sevier River Formation west of the town of Marysvale where kaolinite was mapped using AVIRIS data.

Based on the greater depth of the principal SWIR Al-OH absorption feature of the dickite reference spectrum relative to that of kaolinite (fig. 14b), the results of the ASTER SWIR data analysis shown in figure 13 were reevaluated to examine the relationship of band depth and kandite mineral identification. Gradational stretches were applied to the fit × depth results of pixels matched to well-crystallized kaolinite, and to pixels matched to alunite, alunite + kaolinite, and natroalunite for spatial context (fig. 16a). These stretched results

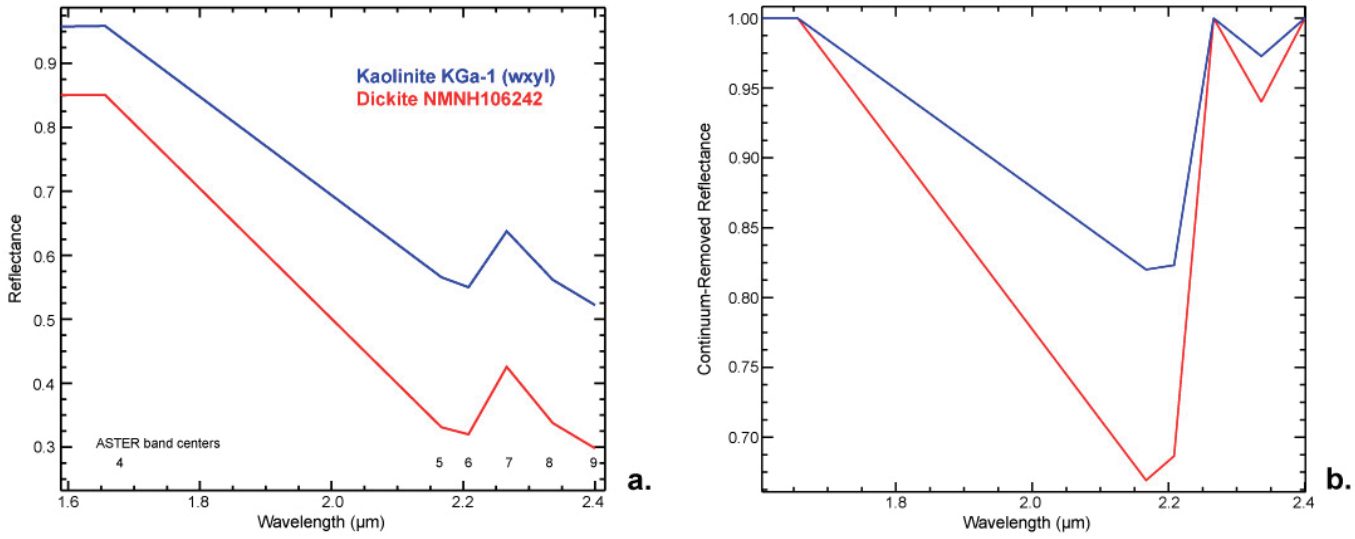


Figure 14. Shortwave infrared spectral plots of dickite and well-crystallized kaolinite from Clark and others (2003b) convolved to ASTER spectral resolution. (a) Reflectance plot showing that the spectral shapes are similar over this spectral range, suggesting that shape alone is insufficient to discriminate the two minerals. (b) Continuum-removed reflectance plot demonstrating that the depth of the 2.2-micrometer Al-OH feature of the dickite spectrum is significantly greater than that of the kaolinite spectrum. PDF version of figure is available **HERE**.

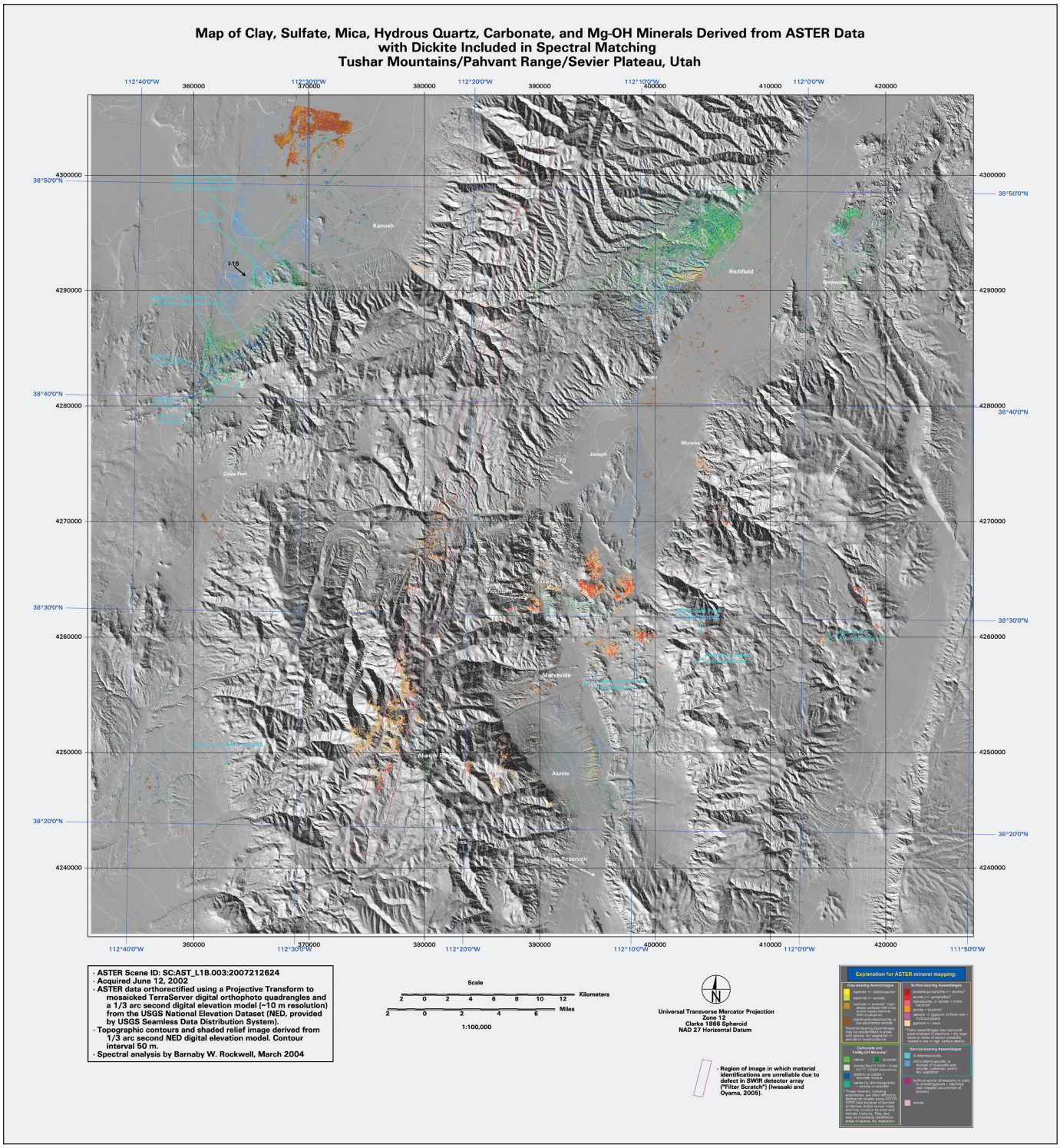


Figure 15. Map of clay, sulfate, mica, hydrous quartz, carbonate, and Mg-OH minerals derived from spectral analysis of ASTER shortwave infrared (SWIR) data with dickite added as a reference spectrum. Larger image is available **HERE**. PDF version of figure is available **HERE**. ERDAS Imagine format data are available **HERE** with material identifications attributed for use in a GIS.

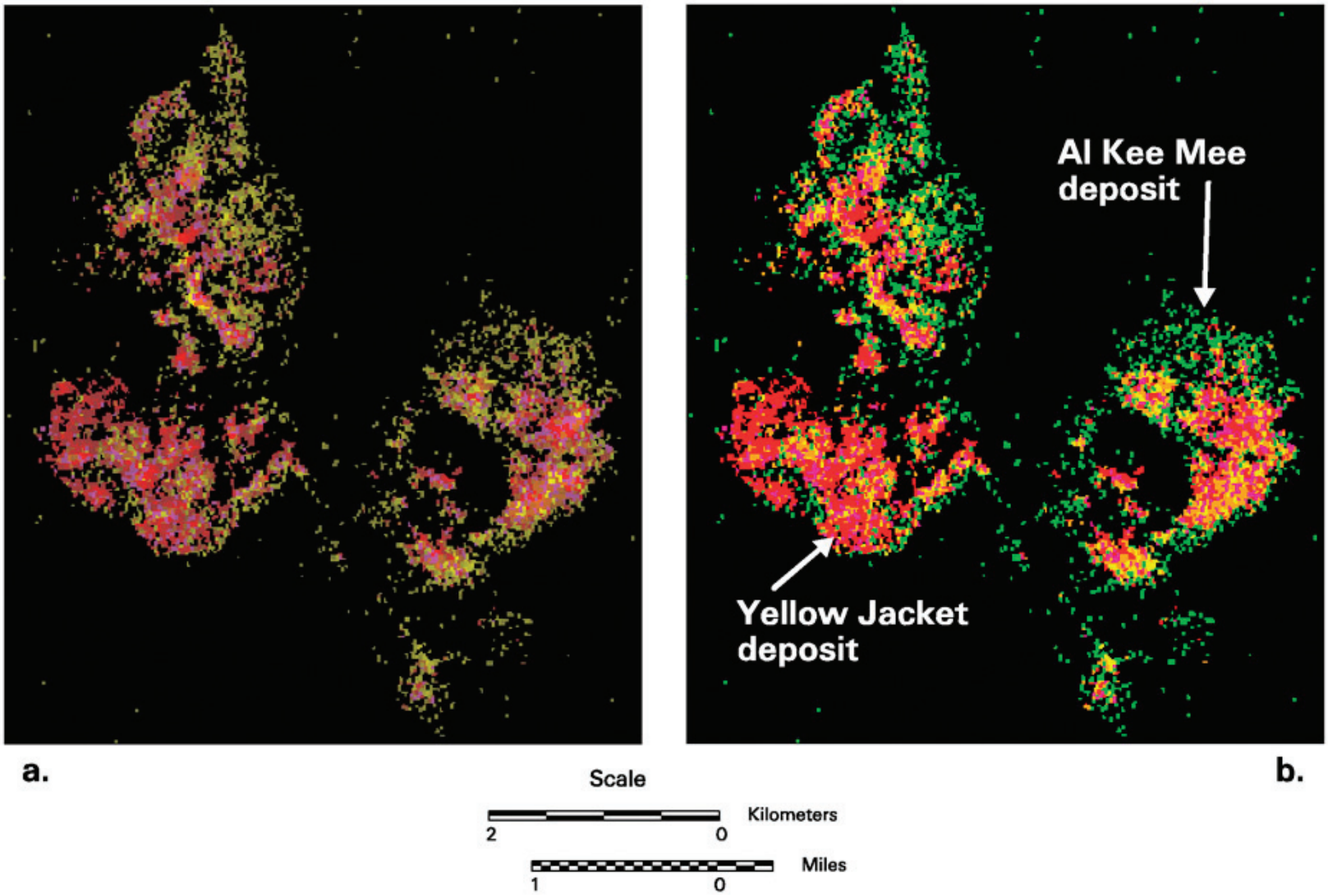


Figure 16. Results of ASTER band depth analysis of mineral identification results shown in figure 13 over the Yellow Jacket and Al Kee Mee replacement alunite deposits in the Antelope Range. (a) Gradationally stretched fit × depth results of pixels matched to alunite (shades of red), alunite + kaolinite (shades of orange), natroalunite (shades of purple), and kaolinite (shades of yellow). Larger image is available **HERE**. ERDAS Imagine format data are available **HERE** with material identifications attributed for use in a GIS. (b) Results from (a) recoded and recolored to highlight kandite mineral differentiation. Pixels matched to alunite shown in red, alunite + kaolinite in orange, and natroalunite in purple. Pixels matched to kaolinite reference spectrum with high fit × depth values (bright shades of yellow in (a) at left) are shown in yellow and are interpreted to represent dickite or well-crystallized kaolinite. Kaolinite matches with lower fit × depth values (darker shades of yellow in (a) at left) are shown in green, and are interpreted as kaolinite, mainly poorly crystallized. Results of (b) covering the entire ASTER scene are shown in figure 17.

were recoded and recolored to highlight the kandite mineral discrimination based on band depth (fig. 16b). Pixels identified as kaolinite with high fit × depth values were colored yellow, and those with lower fit × depth values were colored green. Figure 17 shows these recolored results over the full ASTER scene. Although the kaolinite pixels with high fit × depth values (yellow in fig. 16) generally correspond well with areas in which dickite was detected using AVIRIS data (indicated with magenta circles), some of these pixels correspond to well-crystallized kaolinite ± minor alunite (for example, in the eastern Big Star deposit adjacent to the Antelope mine, figs. 1 and 2). Therefore, these pixels were interpreted as either dickite or well-crystallized kaolinite and occur almost exclusively in areas of hypogene argillic alteration. At the BRCM and White Horse deposits, the dickite and (or) well-crystallized kaolinite pixels correspond with the dickite-bearing argillic selvages identified using AVIRIS data, and the alunite + kaolinite halos around the alunite cores were identified as mixtures of alunite + kaolinite (orange in figs. 13 and 17). Dickite detected using AVIRIS data in altered Navajo Sandstone on the upper northeast and southwest flanks of Deer Trail Mountain, and in related colluvium at the eastern mountain base, was also correctly identified as dickite and (or) well-crystallized kaolinite. Pixels matched to kaolinite with lesser fit × depth values (green in fig. 17) correspond to sedimentary kaolinite in the Crazy Hollow Formation west of Richfield and in kaolinitic areas associated with the alunite deposits. These areas have been interpreted as kaolinite, mainly poorly crystallized and (or) impure (low abundance). Although the kandite mineral discrimination based on band-depth analysis shows promise, substantial errors exist, and the results are useful mainly as a guide for field sampling of high-grade argillic alteration. In addition, as band depth is proportional to material abundance given a constant grain size (Clark, 1999), dickite in low abundance (for example, in alluvium derived from altered areas) may be misidentified as poorly crystallized kaolinite. Figure 18 shows the results of the kandite clay differentiation merged with the standard SWIR mapping results shown in figure 13. Pixels with spectra matched to the reference spectrum of well-crystallized kaolinite (fig. 12) shown in figure 13 have been substituted with (1) the dickite and (or) well-crystallized kaolinite (light pink in fig. 18) and (2) poorly crystallized or impure kaolinite (yellow in fig. 18) derived from the band-depth analysis.

Comparison of AVIRIS- and ASTER-Derived Mineral Maps

Figure 19 shows mineral maps of the White Horse mine area produced from low- and high-altitude AVIRIS data, and the ASTER data. The 3-m pixel size of the low-altitude AVIRIS data (fig. 19a) is well suited for delineating most mappable surface features of the deposit. These data are capable of accurately resolving the clay-free alunite zones at the center of the deposit from the surrounding 14–15-m-wide alunite + kaolinite zone, the 10–11-m-wide "broken clay zone," and outer alunite + kaolinite ± illite zones, which include mine waste rock (Rockwell and others, 2006). These data can also resolve many small, fracture-controlled zones of alunite + kaolinite ± illite surrounded by well-crystallized kaolinite in peripheral areas of the deposit. The typically 2–3-m-wide, fracture-controlled argillic selvages that occur peripheral to the central alunite-bearing zones are typically intimate mixtures of quartz, dickite, and kaolinite, and the low-altitude data are capable of delineating the most dickite-rich zones within the selvages, although pixels identified as dickite and kaolinite usually occur in close juxtaposition to each other.

The high-altitude AVIRIS data (fig. 19b) with 17-m pixel size are capable of delineating the central alunite zone and surrounding alunite + kaolinite transition and argillic zones, the pyritic "proximal propylitic" or phyllic zone that underlies and surrounds the argillic zones, and the "distal" propylitically altered volcanic rocks containing calcite and possible chlorite. However, when compared to the map derived from the low-altitude AVIRIS data, the occurrence of dickite is overestimated at the expense of areal and intimate mixtures of kaolinite ± dickite ± trace alunite, and thus pixels matched to dickite had been labeled as a mineralogically mixed map unit. The 17-m pixel size of the data renders them less capable of resolving the intimate mixtures of dickite and kaolinite in the argillic zones and results in an underestimation of the abundance of kaolinite within them. Nevertheless, analysis of the high-altitude AVIRIS data has clearly identified the halos of dickite-bearing, high-grade argillic alteration in addition to some of the narrow alunite + kaolinite zones surrounded by well-crystallized kaolinite mentioned previously, especially in the volcaniclastic Tmps unit outlined in figure 6.

If the high-grade argillic alteration detected using the band-depth analysis is merged with the standard shortwave-infrared mineral mapping (fig. 18), the ASTER data (fig. 19c) with 30-m pixel size are also capable of delineating most primary deposit features and zoning, but the clay-free central alunite zone (30–32 m wide) cannot be accurately discriminated from the surrounding alunite + kaolinite transition zone because of areal mixing effects. In addition, areal mixing of alunite, clay minerals, and dry vegetation having leaf biochemical absorptions overlapping with the primary sulfate feature of alunite resulted in an overestimation of alunite-bearing mineral assemblages at the expense of clay minerals, mainly kaolinite (for example, localities labeled "1", fig. 19c). Such apparent misidentification of alunite usually occurs at the edges of argillically altered areas where areal mixing with surrounding dry vegetation and soils with dry plant litter can occur. Sensor noise and (or) subtle errors in the reflectance calibration may also contribute to the alunite overestimation. Small, peripheral alunite zones detected with the AVIRIS data also were detected with the ASTER data (locality "2").

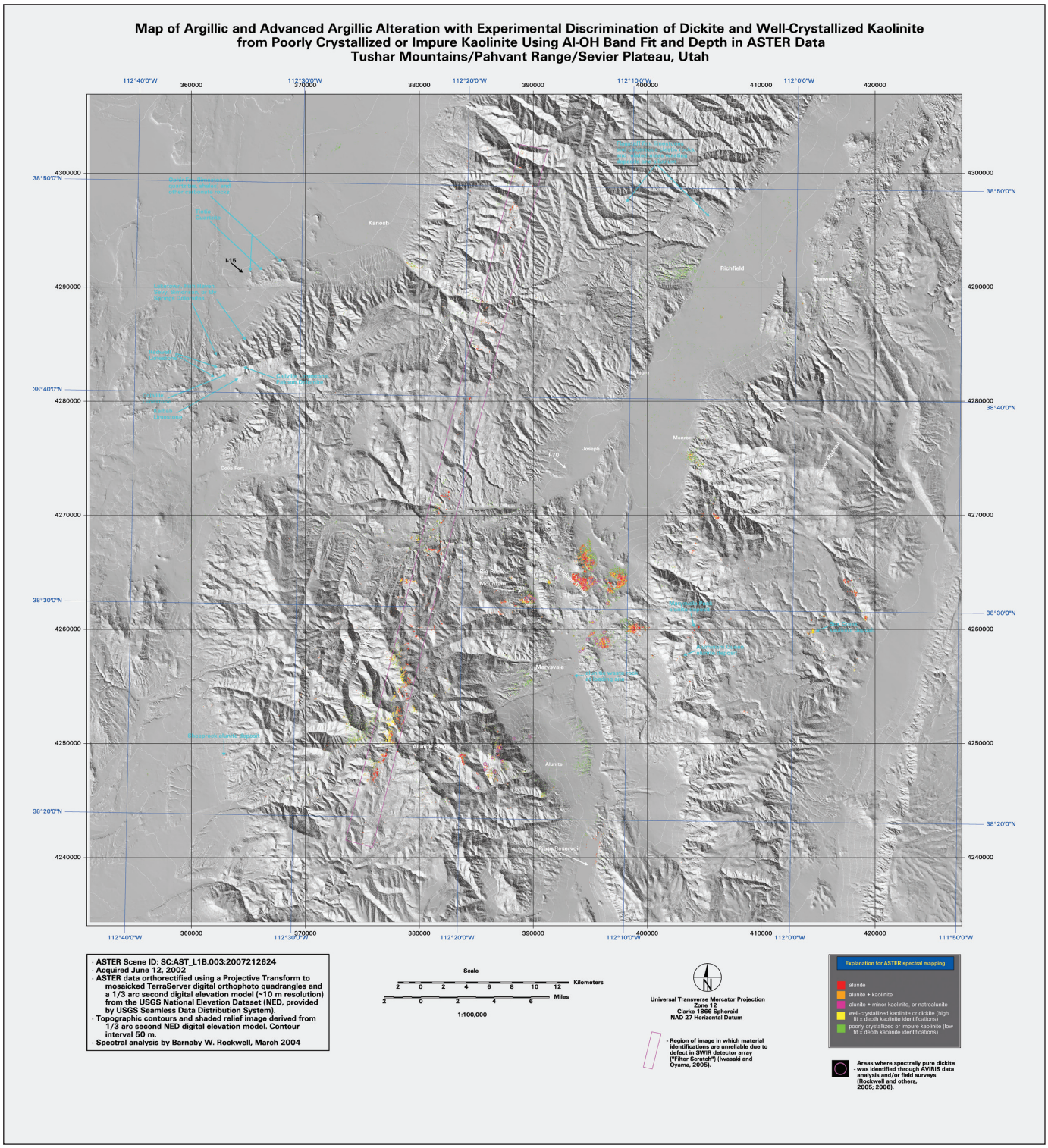


Figure 17. Map of alunites and kandite clay minerals derived from spectral analysis of ASTER shortwave infrared (SWIR) data. Larger image is available **HERE**. PDF version of figure is available **HERE**. ERDAS Imagine format data are available **HERE** with material identifications attributed for use in a GIS. Areas where spectrally pure dickite was identified with AVIRIS data analysis and (or) laboratory analysis of field samples are indicated with magenta circles.

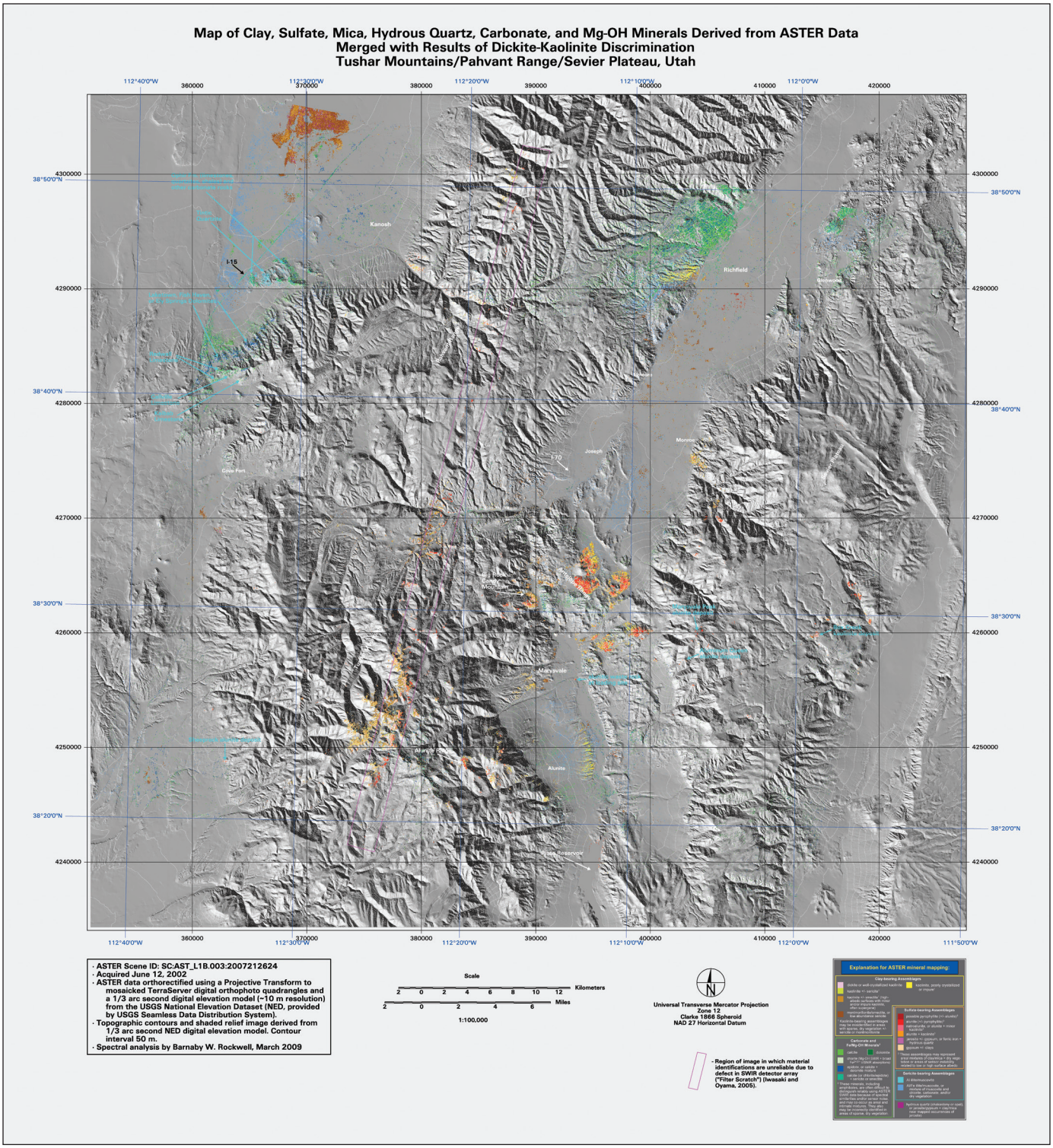
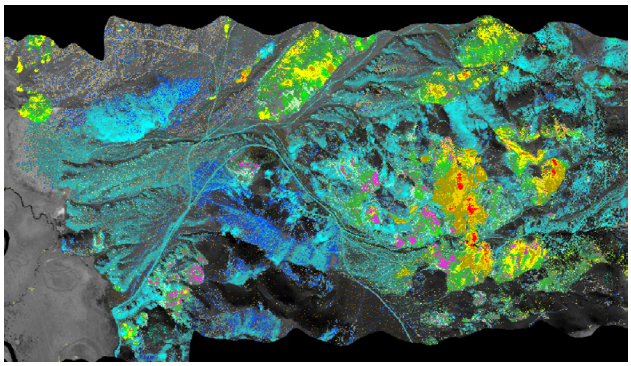
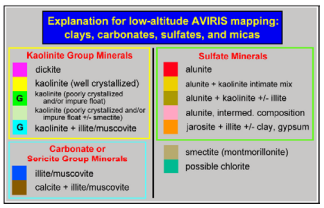
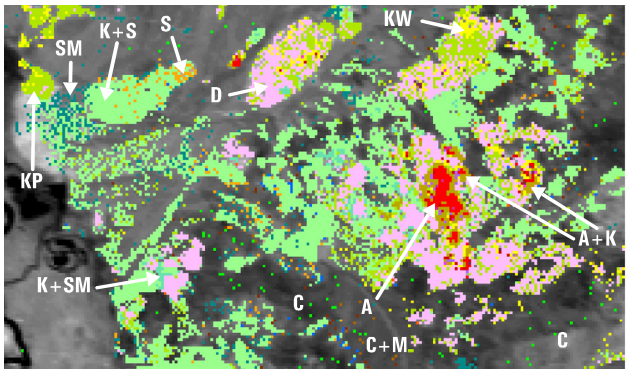


Figure 18. Mineral map from figure 13 merged with results of kandite clay differentiation based on band-depth analysis. Pixels matched to well-crystallized kaolinite shown in yellow in figure 13 have been substituted with (1) dickite and (or) well-crystallized kaolinite (light pink) and (2) poorly crystallized or impure kaolinite (yellow) derived from the band-depth analysis. Larger image is available **HERE**. PDF version of figure is available **HERE**. ERDAS Imagine format data are available **HERE** with material identifications attributed for use in a GIS.



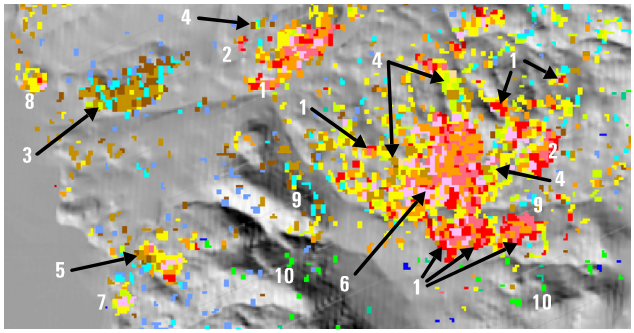


a. Low-altitude AVIRIS mapping results (3-m pixel size)

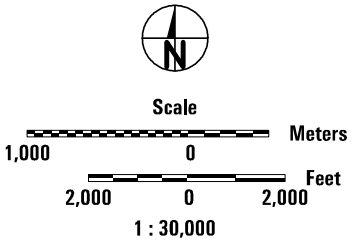


A = alunite
A+K = alunite + kaolinite +/- sericite
D = dickite +/- kaolinite +/- alunite
KW = well-crystallized kaolinite
KP = poorly crystallized or impure kaolinite
K+S = kaolinite + sericite
S = sericite (orange and blue)
K+SM = kaolinite + smectite
SM = smectite (montmorillonite)
C = calcite +/- chlorite (propylitic alteration)
C+M = calcite + muscovite (brown)

b. High-altitude AVIRIS mapping results (17-m pixel size)







c. Merged ASTER mapping results from Fig. 18 (30-m pixel size)

Figure 19. Comparison of shortwave infrared (SWIR) mineral maps derived from AVIRIS and ASTER data. (a) Low-altitude AVIRIS mapping results from figure 6. (b) High-altitude AVIRIS mapping results. PDF version of map with full explanation is available **HERE** (Rockwell and others, 2005). (c) Subset of ASTER mapping results from figure 18. See text for explanation of labeled sites. Larger image is available **HERE**. PDF version of figure is available **HERE**.

Analysis of the ASTER data identified kaolinite + smectite, kaolinite + sericite, sericite, smectite (or low-abundance sericite), and ferric iron minerals (fig. 11) within the proposed relict feeder zone developed in Osiris Tuff 2 km west-northwest of the White Horse mine (fig. 5) within which kaolinite + sericite and sericite in addition to ferric iron minerals were identified with the AVIRIS data (locality "3"). The ASTER data correctly identified the mineral assemblages associated with the weathered "proximal propylitic" or phyllic alteration zone in this area and in other areas closer to the center of the White Horse deposit (locality "4") in which gypsum was also locally detected as it was in similarly altered rocks on the flanks of Big Rock Candy Mountain. The typically supergene clay assemblage kaolinite + smectite was also identified within the Saturday uranium prospect (locality "5") using both the AVIRIS and ASTER data. Low-abundance (low fit × depth) kaolinite + sericite in alluvium derived from the deposit (dark shades of cyan in gradational stretch, fig. 19a) was either not identified using the ASTER data or was removed from the map for the sake of simplicity.

Dickite-bearing, high-grade argillic alteration was identified peripheral to the central alunite-bearing zones (for example, locality "6") and at the Saturday prospect (locality "7") where dickite and kaolinite were detected using the AVIRIS data. Another argillically altered area adjacent to the Sevier River flood plain (locality "8") consisting mainly of kaolinite with local dickite

was identified as containing poorly crystallized kaolinite (yellow in fig. 19c) with local dickite or well-crystallized kaolinite (pink) using the ASTER data. Several pixels with spectra matching the alunite (red) and alunite + kaolinite (orange) reference spectra were also identified in this area using the ASTER data, although no alunite was detected there with the AVIRIS data.

Sericite (cyan in fig. 19c) and local kaolinite + sericite were identified in weakly altered undivided intracaldera intrusions (unit Tmpi, fig. 3) and locally in Osiris Tuff using both the AVIRIS and ASTER data (for example, locality "9"). Calcite and calcite + sericite (muscovite) were identified using all three data types in outlying, propylitically altered areas of these intrusions and in lava flows of Monkey Flat Ridge (unit Tmpf, fig. 3) to the south of the mine (locality "10").

Conclusions

This study demonstrates that methodologies for remote material identification involving continuum removal and least-squares curve fitting designed for analysis of high spectral resolution data can be applied to ASTER multispectral data to efficiently generate maps of surface mineralogy and vegetation groups that are useful for regional hydrothermal alteration detection and characterization and the verification and updating of geologic maps (especially in well-exposed sedimentary terranes). These maps are highly applicable to regional mineral resource assessments and correlate well with more detailed maps generated from analysis of low-altitude AVIRIS data that were used for deposit-scale mapping of mineral zonation related to Miocene advanced argillic alteration and with maps generated from high-altitude AVIRIS data used for a district-scale geoenvironmental study. Concentrations of iron-, clay-, and (or) sulfate-bearing (gypsum and jarosite) minerals formed by supergene weathering of pyritic rocks associated with phyllic alteration (for example, at Big Rock Candy Mountain), alteration associated with Pleistocene to recent hydrothermal activity (for example, Sulphurdale), and pyritic tailings deposits (old Deer Trail mine) were identified using the ASTER data, demonstrating the applicability of ASTER data for regional geoenvironmental assessments.

Acknowledgments

The author thanks the USGS Land Processes Distributed Active Archive Center (LP DAAC), the NASA Earth Observing System Data and Information System (EOSDIS), and the Earth Remote Sensing Data Analysis Center (ERSDAC) of Japan for providing the ASTER data analyzed for this report, and NASA Jet Propulsion Laboratory for providing the AVIRIS data. Thanks also to Albert H. Hofstra and Eric D. Anderson of the USGS for their helpful reviews of this manuscript.

References

Beaty, D.W., Cunningham, C.G., Rye, R.O., Steven, T.A., and Gonzalez-Urien, E., 1986, Geology and geochemistry of the Deer Trail Pb-Zn-Ag-Au-Cu manto deposits, Marysvale district, west-central Utah: Economic Geology, v. 81, no. 8, p. 1932–1952.

Callaghan, Eugene, 1973, Mineral resource potential of Piute County, Utah, and adjoining area: Utah Geological and Mineralogical Survey, Bulletin 102, 135 p.

Church, S.E., Fey, D.L., Klein, T.L., Schmidt, T.S., Wanty, R.B., DeWitt, E.H., Rockwell, B.W., and SanJuan, C.A., in press, Environmental effects of hydrothermal alteration and historical mining on water and sediment quality in central Colorado, *in* Webb, R.M., and Semmens, D.J., Planning for an uncertain future—Monitoring, integration, and adaptation, Proceedings of the Third Interagency Conference on Research in the Watersheds: U.S. Geological Survey Scientific Investigations Report 2009–5049.

Clark, R.N., 1999, Spectroscopy of rocks and minerals, and principles of spectroscopy, *in* Rencz, A.N., ed., Remote sensing for the earth sciences, *in* Ryerson, R.A., ed., Manual of remote sensing, Volume 3: New York, John Wiley, p. 3–58; ***http://speclab.cr.usgs.gov/PAPERS.refl-mrs/refl4.html***.

Clark, R.N., Swayze, G.A., Livo, K.E., Kokaly, R.F., Sutley, S.J., Dalton, J.B., McDougal, R.R., and Gent, C.A, 2003a, Imaging spectroscopy—Earth and planetary remote sensing with the USGS Tetracorder and expert systems: Journal of Geophysical Research, v. 108, no. E12, 5131, doi: 10.1029/2002JE001847.

Clark, R.N., Swayze, G.A., Wise, R., Livo, K.E., Hoefen, T.M., Kokaly, R.F., and Sutley, S.J., 2003b, USGS Digital Spectral Library splib05a: U.S. Geological Survey Open-File Report 2003–395, ***http://pubs.usgs.gov/of/2003/ofr-03-395/ofr-03-395.html***.

Crowley, J.K., and Vergo, N., 1988, Near-infrared reflectance spectra of mixtures of kaolin-group minerals—Use in clay mineral studies: Clays and Clay Minerals, v. 36, no. 4, p. 310–316.

Cunningham, C.G., Rye, R.O., Steven, T.A., and Menhert, H.H., 1984a, Origins and exploration significance of replacement and vein-type alunite deposits in the Marysvale volcanic field, west central Utah: Economic Geology, v. 79, no. 1, p. 50–71.

Cunningham, C.G., Rye, R.O., Rockwell, B.W., Kunk, M.J., and Councell, T.B., 2005, Supergene destruction of a hydrothermal replacement alunite deposit at Big Rock Candy Mountain, Utah—Mineralogy, spectroscopic remote sensing, stable-isotope, and argon-age evidences: Chemical Geology, v. 215, no. 1–4, p. 317–337.

Cunningham, C.G., Steven, T.A., Rowley, P.D., Glassgold, L.B., and Anderson, J.J., 1984b, Map of argillic and advanced argillic alteration and principal hydrothermal quartz and alunite veins in the Tushar Mountains and adjoining areas, Marysvale volcanic field, Utah: U.S. Geological Survey Miscellaneous Investigations Series Map I–1430–B, scale 1:50,000, 1 plate.

Daly, C., Neilson, R.P., and Phillips, D.L., 1994, A statistical-topographic model for mapping climatological precipitation over mountainous terrain: Journal of Applied Meteorology, v. 33, p. 140–158.

Daly, C., Taylor, G.H., and Gibson, W.P., 1997, The PRISM approach to mapping precipitation and temperature, in Reprints—10th Conference on Applied Climatology, Reno, Nevada, American Meteorological Society, p. 10–12.

Ducart, D.F., Crósta, A.P., Filho, C.R.S., and Coniglio, J., 2006, Alteration mineralogy at the Cerro La Mina epithermal prospect, Patagonia, Argentina—Field mapping, shortwave infrared spectroscopy, and ASTER images: Economic Geology, v. 101, no. 5, p. 981–996.

Earth Remote Sensing Data Analysis Center (ERSDAC), 2005, ASTER user's guide, part 1, General, Version 4.0: ***http://www.science.aster.ersdac.or.jp/en/documnts/users_guide/part1/pdf/Part1_4E.pdf***.

Hintze, L.F., Davis, F.D., Rowley, P.D., Cunningham, C.G., Steven, T.A., and Willis, G.C., 2003, Geologic map of the Richfield 30' × 60' quadrangle, southeast Millard county and parts of Beaver, Piute, and Sevier counties, Utah: Utah Geological Survey Map 195, scale 1:100,000, 2 plates, ***http://geology.utah.gov/maps/geomap/30x60/pdf/m-195.pdf***, accessed May 26, 2009, and GIS data available at ***http://ugspub.nr.utah.gov/publications/GIS_maps/Richfield3060.zip***, accessed May 26, 2009.

Iwasaki, A., and Oyama, E., 2005, Correction of stray light and filter scratch blurring for ASTER imagery: IEEE Transactions in Geoscience and Remote Sensing, v. 43, no. 12, p. 2763–2768.

Iwasaki, A., and Tonooka, H., 2005, Validation of a crosstalk correction algorithm for ASTER/SWIR: IEEE Transactions in Geoscience and Remote Sensing, v. 43, no. 12, p. 2747–2751.

Kerr, P.F., Brophy, G.P., Dahl, H.M., Green, J., and Woolard, L.E., 1957, Marysvale, Utah, uranium area—Geology, volcanic relations, and hydrothermal alteration: Geological Society of America Special Paper 64, 212 p.

Kokaly, R.F., Rockwell, B.W., and King, T.V.V., 2006, Characterization of post-fire surface cover, soils, and burn severity at the Cerro Grande fire, New Mexico, using hyperspectral and multispectral remote sensing: Remote Sensing of Environment, v. 106, no. 3, p. 305–325.

Pontual, Sasha, Merry, N., and Gamson, P., 1997, G-Mex—Regolith logging: Kew, Victoria 3101, Australia, Ausspec International Pty., Ltd., v. 8, 60 p.

Rockwell, B.W., 2000, The Goldfield Mining District, Nevada—An acid-sulfate bonanza gold deposit, *in* Floyd F. Sabins, ed., Guidebook for Field Trip to the Basin and Range: Fourteenth International Conference for Applied Geologic Remote Sensing, Las Vegas, Nevada, USA, November 6–8, 2000, 22 p.

Rockwell, B.W., 2002, Descriptions, spectral plots, and digital spectra of samples applied to spectral analysis of imaging spectroscopy data—Utah (East Tintic Mountains, Oquirrh Mountains, Wasatch Mountains, and Tushar Mountains), Nevada (Goldfield Hills), and New Mexico (Jemez Mountains), USA, 1999–2002: U.S. Geological Survey Open-File Report 2002–407, ***http://pubs.usgs.gov/of/2002/ofr-02-407/***.

Rockwell, B.W., 2004, Spectral variations in rocks and soils containing ferric iron hydroxide and (or) sulfate minerals as seen by AVIRIS and laboratory spectroscopy: U.S. Geological Survey Open-File Report 2004–1431, 24 p., ***http://pubs.usgs.gov/of/2004/1431/***.

Rockwell, B.W., Clark, R.N., Cunningham, C.F., Sutley, S.J., Gent, C., McDougal, R.R., Livo, K.E., and Kokaly, R.F., 2000, Mineral mapping in the Marysvale volcanic field, Utah using AVIRIS data, *in* Green, R.O., ed., Summaries of the Ninth Annual JPL Airborne Earth Science Workshop, NASA JPL AVIRIS Workshop, Pasadena, California, U.S.A., February 23–25: JPL Publication 00–18, p. 407–417, ***http://speclab.cr.usgs.gov/earth.studies/Utah-1/marysvale_JPL2000_final.pdf***.

Rockwell, B.W., Clark, R.N., Livo, K.E., McDougal, R.R., and Kokaly, R.F., 2002, AVIRIS data calibration information—Oquirrh and East Tintic Mountains, Utah: U.S. Geological Survey Open-File Report 2002–0200, ***http://greenwood.cr.usgs.gov/pub/open-file-reports/ofr-02-0200/***.

Rockwell, B.W., Cunningham, C.G., Breit, G.N., and Rye, R.O., 2006, Spectroscopic mapping of the White Horse alunite deposit, Marysvale volcanic field, Utah: Evidence of a magmatic component: Economic Geology, v. 101, no. 7, p. 1377–1395.

Rockwell, B.W., and Hofstra, A.H., 2008, Identification of quartz and carbonate minerals across northern Nevada using ASTER thermal infrared emissivity data—Implications for geologic mapping and mineral resource investigations in well-studied and frontier areas: Geosphere, v. 4, no. 1, p. 218–246, doi: 10.1130/GES00126.1, ***http://geosphere.geoscienceworld.org/cgi/content/full/4/1/218***, accessed May 26, 2009.

Rockwell, B.W., and Hofstra, A.H., 2009, Mapping argillic and advanced argillic alteration in volcanic rocks, quartzites, and quartz arenites in the western Richfield 1° × 2° quadrangle, southwestern Utah, using ASTER satellite data, *in* Abstracts with Programs, Geological Society of America Rocky Mountain Sectional Meeting, Orem, Utah, May 11–13, 2009, v. 41, no. 6, p. 39, ***http://gsa.confex.com/gsa/2009RM/finalprogram/abstract_157802.htm***, accessed May 26, 2009.

Rockwell, B.W., McDougal, R.R., and Gent, C.A., 2005, Remote sensing for environmental site screening and watershed evaluation in Utah mine lands—East Tintic Mountains, Oquirrh Mountains, and Tushar Mountains: U.S. Geological Survey Scientific Investigations Report 2004–5241, 84 p., ***http://pubs.usgs.gov/sir/2004/5241/*** and ***http://speclab.cr.usgs.gov/earth.studies/Utah-1/sir5241txto_bredit.html***.

Rowley, P.D., Cunningham, C.G., Steven, T.A., Workman, J.B., Anderson, J.J., and Theissen, K.M., 2002, Geologic map of the central Marysvale volcanic field, southwestern Utah: U.S. Geological Survey Geologic Investigations Series I–2645–A, scale 1:100,000, ***http://greenwood.cr.usgs.gov/pub/i-maps/i-2645-a/***.

Williams, P.E. and Hackman, R.J., 1971, Geology of the Salina quadrangle, Utah: U.S. Geological Survey Miscellaneous Geologic Investigations Map I–591–A, scale 1:250,000, 1 plate, ***http://ngmdb.usgs.gov/Prodesc/proddesc_9374.htm*** and ***http://geology.utah.gov/maps/geomap/1x2/pdf/i-591.pdf***.

Publishing support provided by:
Denver Publishing Service Center, Denver, Colorado
Manuscript approved for publication, May 29, 2009
Edited by Mary A. Kidd
Layout by Joy Monson

For more information concerning this publication, contact:
Team Chief Scientist, USGS Central Mineral Resources
Box 25046, Mail Stop 973
Denver, CO 80225
(303) 236-1562

Or visit the Central Mineral Resources Team Web site at:
http://minerals.cr.usgs.gov/

This publication is available online only at:
http://pubs.usgs.gov/sir/2009/5117/

